Materials Advances

REVIEW

View Article Online
View Journal

Cite this: DOI: 10.1039/d5ma01482d

Lead-free metal halide layered double perovskites as sustainable platforms: composition tuning, synthetic methods and advanced applications

Kavitha H.,[a] Sangita Das[b] and Partha Pratim Das*[a]

Received 18th December 2025,
Accepted 19th May 2026

DOI: 10.1039/d5ma01482d

rsc.li/materials-advances

The growing demand for environmentally friendly and stable materials has accelerated research into lead-free alternatives for optoelectronic and energy applications. Among these, layered double perovskites (LDPs) with the general formula $A_4B(\text{II})B(\text{III})_2X_{12}$ have gained attention due to their structural versatility, tunable optoelectronic properties and enhanced stability. This review critically examines compositional engineering in mixed-metal halide LDPs, focusing on how targeted modification of cationic and anionic sublattices governs their optoelectronic behaviour. The molecular source of band gap tunability, photoluminescence properties, defect tolerance, and structural stability are highlighted, providing a unified perspective on structure–property correlations in this material class. The impact of synthetic techniques is further investigated, demonstrating how regulated crystallisation pathways from bulk and single crystals to nanostructures and thin films dictate morphology, defect landscape, and phase purity, ultimately determining material performance. The integration of composition design with synthesis control has been demonstrated to be necessary for unlocking the full potential of LDPs. Recent advances in the applications of tailored LDP compositions in energy conversion and optoelectronic devices are discussed to illustrate their growing technological relevance. Overall, this review aims to provide a unified understanding of the structure–property–function relationship in lead-free LDPs, while also identifying future directions for high-performance, environmentally benign lead-free perovskite-based systems.

---

[a] *Manipal Institute of Technology, Manipal Academy of Higher Education, Manipal-576104, Karnataka, India. E-mail: partha.das@manipal.edu*
[b] *Department of Biochemistry, School of Chemical Sciences, St Joseph's University, Bengaluru-560027, Karnataka, India*

Kavitha H.

Kavitha Hosamane is a PhD student at Manipal Institute of Technology, Manipal Academy of Higher Education (MAHE), Manipal, India. She obtained her master's degree in Organic Chemistry in 2024 from SDM College, Ujire, Karnataka, India. In 2024, she commenced her PhD at MAHE under the supervision of Dr Partha Pratim Das. Her research focuses on lead-free metal halide perovskites for optoelectronic applications.

Sangita Das

Dr Sangita Das is an Assistant Professor at St. Joseph's University, Bangalore, India. Her research interests include organic and supramolecular chemistry, fluorescence sensing, molecular recognition, advanced functional materials, and drug delivery systems. She completed her PhD from the Indian Institute of Engineering Science and Technology, Shibpur, India under the CSIR-JRF programme in 2011. She was awarded the prestigious Newton International Fellowship and conducted research at Durham University, UK (2019–2021), followed by research activities at KIST Europe, Germany in 2022. She has published extensively in reputed international journals and edited scientific books in sensing and biomedical materials.

1. Introduction

1.1 Metal halide perovskites

Recently, metal halide perovskites have turned out to be the most promising class of functional materials for various applications, including photocatalytic CO_2 reduction, photovoltaic (PV) cells, light emitting diodes (LEDs), photodetectors, lasers and scintillators owing to their remarkable optical and electronic properties as well as their ease of solution processibility.[1–3]

The basic perovskite structure follows the general formula ABX_3, where B is a divalent cation that occupies the BX_6 octahedral center and A is a monovalent cation that occupies the interspace of the octahedral BX_6 framework coordinated with X anions. The metal halide perovskites show excellent optoelectronic properties such as optical absorption, narrow band gaps, superior charge carrier mobility, photoluminescence, defect tolerance, conductivity, *etc.*[4,5] As reflected by the strong broad absorption in the visible region of the solar spectrum, metal halide perovskites possess outstanding optical absorption property that can be utilized for visible light optoelectronics.[6] A notable example is methylammonium lead iodide ($MAPbI_3$), one of the extensively explored perovskite materials in various applications including photovoltaic cells, photodetectors and LEDs owing to its excellent optoelectronic properties.[7–9]

Despite the rapid increase in the power conversion efficiency of the lead-based perovskites in a short period of time, they face many challenges. The first drawback of lead-based perovskites is the degradation of the compound upon exposure to oxygen and moisture.[10] The one more major drawback is its toxicity. The lead metal we get from earth crust is toxic, but the lead halide that is formed as the degradation product of metal halide perovskites is even more toxic than the lead metal.[11] Researchers have found several ways of replacing lead to develop non-toxic, stable and highly efficient perovskite materials.

To replace toxic Pb^{2+} in perovskites, isoelectronic cations such as Sn^{2+} and Ge^{2+} have been explored due to their similar outer ns^2 electronic configuration. Sn-based perovskites showed narrower optical bandgaps and high carrier mobilities compared to the lead-based perovskites. Nevertheless, the instability of Sn^{2+} prone to oxidation leads to the formation of vacancies, which promote charge carrier recombination and degrade performance. However, no other divalent cations showed suitable optical activity in replacement of lead.[12,13] To synthesize a stable perovskite the ionic radius and charge neutrality conditions must be considered. The octahedral factor (R_B/R_X) must be within the range of 0.44 to 0.90 and the tolerance factor of the material should be in the range of 0.813 to1.107 to get a stable perovskite structure. The tolerance factor can be calculated by using the formula $(R_A + R_X)/2[R_B + R_X]$, where R_A, R_B and R_X are the ionic radii of the A-site cation, B-site cation, and X-site anion respectively.[10]

In pursuit of environmentally benign and stable alternatives to lead-based perovskites, less toxic trivalent cations such as Bi^{3+} and Sb^{3+} have emerged as promising candidates giving rise to the layered structure with the formula $A_3B_2X_9$. Bismuth-based perovskites, in particular, have demonstrated superior stability compared to their lead-containing counterparts.[14] However, their optoelectronic performance remains limited due to intrinsic challenges, including indirect and wide bandgaps, large carrier effective masses, low carrier mobility, and poor defect tolerance.[15] Antimony is in the same group as that of bismuth and can be a good replacement of lead as it has outer ns^2 configuration as in the case of lead. The zero-dimensional dimer phase of antimony-based compounds suffers from indirect band gaps and low carrier transport.[16] The two-dimensional layered phase shows better performance compared to the dimer phase. Nevertheless, the efficiency of antimony-based perovskites remains modest. Recent efforts have focused on band gap engineering particularly through doping strategies to optimize absorption in alignment with the solar spectrum.[17] In addition to heterovalent replacement, another promising approach for mitigating the limitations of lead-based perovskites involves the development of double perovskite structures.[18,19] In this strategy, two divalent lead ions are replaced either by the vacancy ordered tetravalent metal ions or by the combination of trivalent and monovalent ions, resulting in compounds with general formulas $A_2B(\text{IV})X_6$ and $A_2B(\text{I})B(\text{III})X_6$ respectively.[20–22] There is still scope for the discovery of new materials based on incorporation of different combinations of metals for the betterment of optoelectronic properties.

1.2 Layered double perovskites (LDPs)

LDPs represent an emerging class of lead-free halide perovskites formed by combining heterovalent cation substitution, with dimensional reduction of three-dimensional double perovskite frameworks. This design strategy enhances compositional diversity, structural stability, and tunability of

Partha Pratim Das

Dr Partha Pratim Das is an Assistant Professor at the Manipal Institute of Technology, Manipal Academy of Higher Education, Manipal, India. He received his PhD in Chemistry from Jadavpur University, Kolkata, India in 2016, with research conducted at CSIR-Central Glass and Ceramic Research Institute, Kolkata and CSIR-National Chemical Laboratory, Pune, India. He subsequently pursued postdoctoral research at Yonsei University and Seoul National University, South Korea under nationally funded research programmes (2016–2022). His research focuses on the processing, structure, and optoelectronic properties of advanced functional materials under varied conditions, with particular emphasis on sustainable energy and environmental applications.

optoelectronic properties. LDPs can be broadly classified based on their crystallographic orientation (*e.g.*, 100 and 111 oriented structures) as well as the nature of the spacer cations.[4] In particular, LDPs incorporating organic spacer cations form hybrid structures that are further categorised into Ruddlesden–popper (RP) and Dion–Jacobson (DJ) phases, depending on whether monovalent or divalent organic spacers are present. These organic–inorganic hybrid LDPs offer additional flexibility in tuning interlayer interactions, octahedral distortions and electronic properties.[23] In contrast, fully inorganic LDPs typically exhibit improved thermal and environmental stability. Among the various compositions, 111 oriented LDPs with the general formula $A_4B(\text{II})B(\text{III})_2X_{12}$ have attracted particular attention due to their structural simplicity, enhanced stability, and promising optoelectronic characteristics.[2]

1.3 $A_4B(\text{II})B(\text{III})_2X_{12}$ family of materials

The LDPs having the general formula $A_4B(\text{II})B(\text{III})_2X_{12}$ have emerged considering the advantages of both layered and double perovskites to give the combined improvement in stability and optoelectronic properties as illustrated in Fig. 1. Here, the A-site typically denotes a monovalent cation, while B(II) and B(III) are divalent and trivalent metal cations, respectively, coordinated by halide ions.[2,24] Based on the presence of four A-site cations in their chemical formula, these LDPs are commonly referred to as quadruple perovskites. These compounds form a layered architecture with alternating metal-halide octahedral sheets, differing from the classical 3D perovskites while offering a tunable lattice framework. Such configurations have been explored primarily in compositions like $Cs_4Cu(\text{II})Sb_2(\text{III})Cl_{12}$ which is a very first member of this family.[25] While lead free strategies address toxicity in halide perovskites, all inorganic heterometallic $A_4B(\text{II})B(\text{III})_2X_{12}$ LDPs stand out for their large compositional space, tunable optoelectronic properties, enhanced structural stability and their potential application in various emerging fields. These traits position LDPs as superior alternatives when compared to other lead-free perovskites.[26]

The possibility of forming these quadruple perovskite crystal structures and their phase stability can be predicted by the modified Goldschmidt parameters specific to the $A_4B(\text{II})B(\text{III})_2X_{12}$ family of materials; and DFT calculations can be used to investigate the thermodynamic stability and to know the degradation products.[4]

$$\text{Effective tolerance factor, } t_{\text{eff}} = \frac{R_A + R_X}{\sqrt{2\left\{\frac{R_{B^{\text{II}}} + R_{B^{\text{III}}}}{3} + R_X\right\}}}, \ [0.81 < t_{\text{eff}} < 1.11], \quad (1)$$

$$\text{Effective octahedral factor, } \mu_{\text{eff}} = \frac{R_{B^{\text{II}}} + R_{B^{\text{III}}}}{3R_X}, \ [0.41 < \mu_{\text{eff}} < 0.90], \quad (2)$$

where R_A, $R_{B^{\text{II}}}$, $R_{B^{\text{III}}}$ and R_X are the ionic radii of A B^{II} B^{III} and X respectively.

To date, a wide range of compositions and synthetic strategies have been developed to create LDPs with diverse morphologies. They are extremely adaptable candidates for incorporation into a variety of applications due to their vast compositional flexibility and customizable optoelectronic capabilities. Despite these benefits, $A_4B(\text{II})B(\text{III})_2X_{12}$ LDPs encounter several interrelated difficulties. The accessible compositional space remains relatively small, and many materials exhibit unfavourable band structures limiting their optoelectronic performance. Furthermore, problems with crystallization control, defect tolerance, and film integrity continue to make it difficult to produce homogeneous, device-quality thin films, which impedes practical application and results in inconsistent and fragmented reports in the literature. In this regard, a targeted review is necessary to critically integrate current research, establish

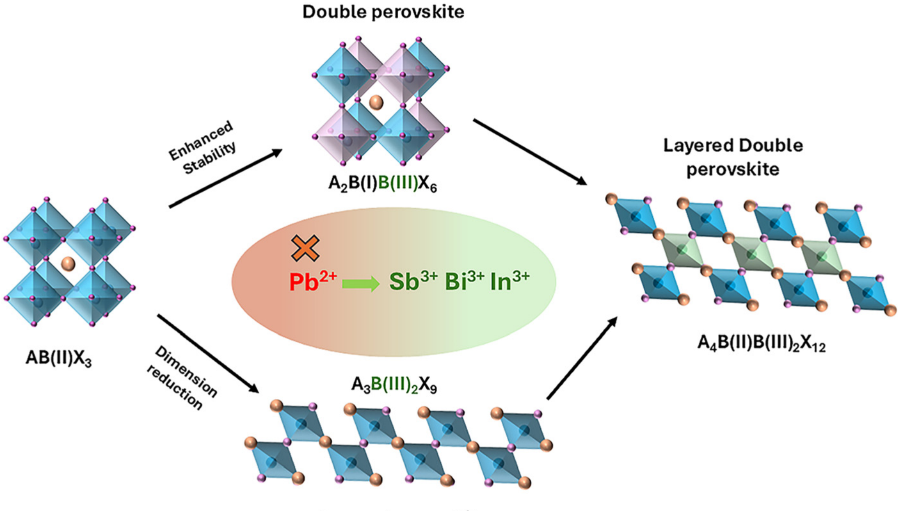

Fig. 1 Schematic showing the emergence of $A_4B(\text{II})B(\text{III})_2X_{12}$ metal halide layered double perovskites.

composition–property correlations, and emphasize practical methods for compositional adjustment and material synthesis.

Previous reviews on LDPs have addressed different aspects of this material class but remain limited in scope with respect to the 111-$A_4B(\text{II})B(\text{III})_2X_{12}$ family. For instance, in the review written by Vargas *et al.*, primary focus is placed on the structural evolution of LDPs, with significant emphasis on 100 oriented systems, while the compositional diversity of the 111 family is briefly highlighted.[4] In addition, in a broader review written by Nie *et al.*, lead-free materials are mainly focused with the emphasis on solar cell applications.[27] Similarly, in the work by Lee *et al.*, attention is concentrated on narrow band gap halide double perovskites, particularly $Cs_4CuSb_2Cl_{12}$, with an application-driven perspective centred on band gap engineering.[6] Although a more direct discussion on this family is provided by Cai *et al.*, the treatment of compositional tunability across A-, B-, and X-sites, as well as synthesis–structure–property correlations, remains limited.[2] Furthermore, in a more recent review by Ghasemi *et al.*, major focus is placed on organic spacer-based LDPs.[23]

In this context, we mainly concentrate on recent advancements in $A_4B(\text{II})B(\text{III})_2X_{12}$ LDPs, covering important discoveries made over the last five to ten years. This review starts with a thorough introduction to compositional engineering in LDPs, with a focus on changes at the A-, B-, and X-sites and how these affect structural, optical, and electrical properties. To give a better grasp of the links between structure and properties, ideas from computational studies on compositional tuning are also explored. The subsequent section thoroughly examines the synthetic techniques used to produce LDPs in different morphologies including bulk materials, single crystals, nanocrystals, and thin films with special attention to how synthesis methods impact optoelectronic performance. This is followed by a description of recent developments in LDP applications, including optoelectronics, photocatalytic CO_2 reduction, and photo-thermoelectric energy conversion. Finally, this study offers guidelines on the rational design and development of next-generation lead-free perovskite materials by describing important challenges and potential opportunities.

2. Compositional tuning in LDPs

Compositional tuning in LDPs has become a potent method for precisely regulating their structural, electrical, and optical characteristics. Doping or alloying cations at different lattice sites can change important properties like the band gap, photoluminescence, and charge carrier dynamics. This tunability enables the design of perovskite materials with tailored functionalities for applications in optoelectronics and energy conversion. Variations at the monovalent and divalent sites strongly influence dimensionality and electronic configuration, offering versatile pathways to enhance stability and performance in LDP systems. The recent progress in compositional tuning, synthesis and applications of LDPs is summarised in Tables 1 and 2.

2.1 A-Site engineering

The A-site cation fills the cavities generated by the corner-sharing BX_6 octahedral framework in metal halide perovskites. It acts primarily as a structural template, supporting the lattice while maintaining overall charge neutrality. The geometric compatibility between the A-site cation and the BX_6 framework significantly impacts the structural symmetry and stability of the perovskite lattice.[78] The size of the A-site cation and how it interacts with nearby halide ions can have a significant effect on the crystal structure, octahedral distortion, and the optoelectronic properties that go along with them.[78,79]

The structural stability of perovskite materials is often assessed using the Goldschmidt tolerance factor, which is determined by the ionic radii of the A, B, and X-site ions. A tolerance factor close to one helps to create a perfect cubic structure with little distortion of the lattice. On the other hand, deviations from this range can cause octahedral tilting and structural distortions that change the material's electronic band structure and optical properties.[80,81] Even though A-site cations usually don't have much of an effect on the frontier electronic states near the band edges, their indirect effect on the geometry of the lattice can have a big impact on carrier transport, band gap energy, and excitonic properties. Consequently, a-site engineering has developed into a proficient method for customizing the structural and optoelectronic properties of metal halide perovskites.[79,82]

The caesium ion is the most used A-site cation in layered double perovskites, primarily due to its suitable ionic radius. However, Gray *et al.* (2021) successfully demonstrated the substitution of caesium with rubidium, synthesizing two new compounds $Rb_4CuSb_2Cl_{12}$ and $Rb_4MnSb_2Cl_{12}$ using a glove box setup.[56] Substituting rubidium for caesium is expected to enhance longer wavelength light absorption and reduce the density of defect states, while preserving the integrity of the crystal lattice. For example, Rb-doped $Cs_2AgBiBr_6$ devices demonstrated an average power conversion efficiency (PCE), nearly 15% higher than that of undoped counterparts. Despite this achievement, further investigation of these materials is limited by their extreme sensitivity to moisture.[83,84]

One widely used approach for A-site tuning is cation substitution, in which the original A-site ion is replaced by another monovalent cation with a different ionic radius. Such substitutions can alter lattice parameters, induce octahedral tilting and tune the electronic band structures of the material. Another strategy involves A-site alloying, where two or more a-site cations are incorporated simultaneously to form mixed cation systems. In these systems, the effective ionic radius of the A-site can be controlled through compositional tuning, thereby enabling systematic adjustment of the tolerance factor and crystal symmetry. This approach has been widely used to improve structural stability and suppress defect formation in perovskite materials.[27,79]

A-site engineering can also influence the dimensionality of perovskite structures. Incorporating larger organic cations can disrupt the three-dimensional framework, yielding quasi-two-dimensional or layered structures with enhanced environmental

Table 1 Summary of reported synthetic routes, properties and applications of $Cs_4CuSb_2Cl_{12}$ and its derivatives

Author (year)	Composition/ morphology	Structure/space group	Method	Band gap/ emission	Application/key performance	Ref.
Vargas (2017)	$Cs_4CuSb_2Cl_{12}$ MCs	Monoclinic ($C2/m$)	Acid precipitation	1 eV	Narrow bandgap	25
Singhal (2018)	$Cs_4CuSb_2Cl_{12}$ MCs	Monoclinic ($C2/m$)	Mechanochemical	1.1 eV	Reversible thermal changes	28
Wang *et al.* (2019)	$Cs_4CuSb_2Cl_{12}$ NCs	Monoclinic ($C2/m$)	Ultrasonic Exfoliation	1.6 eV ~630 nm	Photoelectrochemical application	29
Cai *et al.* (2020)	$Cs_4CuSb_2Cl_{12}$ NCs	Monoclinic ($C2/m$)	Hot injection	1.79 eV	Photodetectors (a lifetime of ~150 ps)	30
Jayasankar *et al.* (2020)	$Cs_4CuSb_2Cl_{12}$ MCs	Monoclinic ($C2/m$)	Precipitation in ethanol	1.16 eV	Photodetectors (a responsivity of 10^{-3} A W^{-1} and a detectivity of 10^8 J)	31
Cai *et al.* (2021)	$Cs_4Cu_{1-x}Cd_xSb_2Cl_{12}$ NCs	Trigonal ($R\bar{3}m$) to monoclinic ($C2/m$)	Hot injection	3.19–1.92 eV	Photodetectors (rise time ~25 ps and lifetime ~150 ps)	32
Ashitha *et al.* (2021)	$Cs_4CuSb_2Cl_{12}$ NCs	Monoclinic ($C2/m$)	Hot injection method	1.56 eV 570 nm (weak)	Photocatalyst in ferricyanide reduction and dye degradation	33
Mandal *et al.* (2022)	$Cs_4CuSb_2Cl_{12-x}I_x$ NCs	Monoclinic ($C2/m$)	Hot injection method	1.96–1.92 eV 446–479 nm	Photodetectors (a responsivity of 0.67 A W^{-1} and a detectivity of 4.55×10^8 Jones)	34
Parveen (2022)	$Cs_4CuSb_2Cl_{12}$ MCs, NCs and thin film	Monoclinic ($C2/m$)	Mechano chemical and solvothermal	1.32 eV (MC) 2.2 eV (NC) 1.1 eV (film)	Analog memristor	35
Wu *et al.* (2022)	$Cs_4CuSb_2Cl_{12}$ MCs & QDs	Monoclinic ($C2/m$)	Acid precipitation Hot injection	1.40 eV 1.67 eV	Photocatalytic CO_2 reduction (CO yield of 233 μmol g^{-1} after 3 h of illumination)	36
Zhang *et al.* (2023)	$Cs_4CuSb_2Cl_{12}$ MCs	Monoclinic ($C2/m$)	Acid precipitation	0.88 eV	Q-switched mode-locking fibre laser	37
Vahid *et al.* (2023)	$Cs_4CuSb_2Cl_{12}$ MCs	Monoclinic ($C2/m$)	Precipitation method	1.10 eV	Stabilizer in a solar cell device	38
Mishra *et al.* (2023)	$Cs_4CuSb_2Cl_{12}$ MCs	Monoclinic ($C2/m$)	Precipitation method	1.66 eV	Solvent dependent relaxation rates of carriers	39
Balderas *et al.* (2023)	$Cs_4CuSb_2Cl_{12}$ $Cs_4CuSb_2Cl_{12}$:F^- thin film	Monoclinic ($C2/m$)	Vapour deposition method	1.65–1.70 eV	Photodetector and memdiodes (conductivity 1.94×10^{-5} S cm^{-1})	40
Zhang *et al.* (2024)	$Cs_4CuSb_2Cl_{12}$ MCs	Monoclinic ($C2/m$)	Ball milling	1.084–1.066–1.029 eV	Photocatalytic CO_2 reduction (CO yield of 72.17 μmol g^{-1} after 4 h of irradiation)	41
Wang *et al.* (2024)	$Cs_4CuSb_2Cl_{12}$ MCs	Monoclinic ($C2/m$)	Acid precipitation	1.01 eV	Photothermal production of H_2	42
Pritam *et al.* (2024)	$Cs_4CuSb_2Cl_{12}$	Monoclinic ($C2/m$)	Theoretical study	1.6 eV	Device engineering	43
Mishra *et al.* (2025)	$Cs_4CuSb_2Cl_{12}$ MCs	Monoclinic ($C2/m$)	Solution processed method	1.57	Surface passivation	44
Chang *et al.* (2025)	$Cs_4Cu_{1-x}Cd_xSb_2Cl_{12}$ $Cs_4Cu_{1-y}Mn_ySb_2Cl_{12}$ MCs	Monoclinic ($C2/m$) to trigonal ($R\bar{3}m$)	Acid precipitation method	1–2.95 eV	Band gap tuning	45
Sridhar *et al.* (2025)	$Cs_4CuSb_2Cl_{12}$ MCs/MoS_2	Monoclinic ($C2/m$)	Precipitation method	1.1 eV	Photothermal energy conversion	46
Sarkar *et al.* (2025)	$Cs_4CuSb_2Cl_{12}$ MCs	Monoclinic ($C2/m$)	Acid precipitation	0.9 eV	Humidity and temperature sensing	47

stability and promising optoelectronic properties.[4] In the case of $A_3Sb_2I_9$, when the bulky organic group methyl ammonium (MA^+) was substituted in the A-site, the hybrid antimony perovskite ($MA_3Sb_2I_9$) adopted the dimer structure(0D), while the inorganic $Cs_3Sb_2I_9$ with Cs^+ at the A-site followed the layered structure. These structural alterations frequently result in increased moisture stability and tunable optical characteristics, which are useful for optoelectronic applications.[85]

Despite these benefits, several challenges remain in the implementation of A-site engineering strategies. The strict geometric constraints of the perovskite lattice pose a major limitation, as unsuitable ionic sizes can cause structural instability or the creation of non-perovskite phases. Furthermore, in mixed-cation systems, phase segregation or compositional inhomogeneity may arise, compromising the long-term stability and reproducibility of material properties. Variations in the A-site ionic radius can impact interlayer distance, lattice distortion, and octahedral connectivity, hence influencing the material's electrical structure and optical performance. For example, in Cs-based LDPs like $Cs_4CuSb_2Cl_{12}$, the Cs^+ ions provide structural stabilization to the layered lattice while retaining charge balance within the framework.

Beyond single A-site cation systems, multi-cation approaches present a promising pathway for fine tuning the characteristics of $A_4B(\text{II})B(\text{III})_2Cl_{12}$ LDPs. Recent research on mixed A-site antimony halides such as $A_{3-x-y}A'_xA''_ySb_2X_9$ reveals that introducing different monovalent cations, including caesium, methylammonium, formamidinium and rubidium ions, can efficiently control lattice parameters, structural stability and optoelectronic capabilities.[86,87] Inspired by these developments, similar A-site compositional engineering could be extended to LDPs. Partial replacement of the Cs^+ with other monovalent cations may enable modulation of octahedral distortion, band structure, and charge carrier dynamics, opening new avenues for optimizing the performance of $A_4B(\text{II})B(\text{III})_2Cl_{12}$ LDPs for optoelectronic and energy conversion applications.

2.2 B(II)-site engineering

In $A_4B(\text{II})B(\text{III})_2X_{12}$ LDPs, the B(II) site plays an important role in determining the electronic structure, optical absorption, and

Table 2 Summary of reported synthetic routes, properties and applications of Cd-, Mn- and other transition metal-based layered double perovskites

Author	Composition/morphology	Structure (space group)	Synthesis	Band gap/ emission	Application/key performance	Ref.
Vargas *et al.* (2018)	$Cs_4Mn_{1-x}Cu_xSb_2Cl_{12}$ MCs	Trigonal ($R\bar{3}m$) to monoclinic ($C2/m$)	Acid precipitation	3–1 eV 605 nm	Band gap tuning	24
Lin *et al.* (2019)	$Cs_4CdBi_2Cl_{12}$ $Cs_4CdSb_2Cl_{12}$ SCs	Cubic ($Fd\bar{3}m$)	Solvothermal	3.0–3.23 eV 700 nm	Orange emission	48
Vargas *et al.* (2020)	$Cs_4Cd_{1-x}Mn_xBi_2Cl_{12}$ MCs	Trigonal ($R\bar{3}m$)	Acid precipitation	3.2–3.1 eV 595 nm	Enhanced luminescence (PLQY-79.5%)	49
Holzapfel *et al.* (2020)	$Cs_4Cd_{1-x}Mn_xBi_2Cl_{12}$ SCs	Trigonal ($R\bar{3}m$)	Hydrothermal	3.2 eV 605 nm	Orange red emission PLQY-57%	50
Wei *et al.* (2020)	$Cs_4MnBi_2Cl_{12}$ MCs & SCs	Trigonal ($R\bar{3}m$)	Acid precipitation solvothermal	610 nm	X-ray scintillator (PLQY-25.7%)	51
Yang *et al.* (2020)	$Cs_4(Cd_{1-x}Mn_x)Bi_2Cl_{12}$ NCs	Trigonal ($R\bar{3}m$)	Hot injection method	3.49–3.56 eV ∼602 nm	Mn–Mn coupling interaction (PLQY $< 0.1\%$)	52
He *et al.* (2021)	$Cs_4Mn(Bi_{1-x}In_x)_2Cl_{12}$ MCs	Trigonal ($R\bar{3}m$)	Acid precipitation	606–616 nm	LED	53
Ma *et al.* (2021)	$Cs_4MnBi_2Cl_{12}$ SCs	Trigonal ($R\bar{3}m$)	Hydrothermal	3.26–2.0 eV 600 nm	Pressure induced band gap tuning	54
Bai *et al.* (2021)	$Cs_4M(II)Bi_2Cl_{12}$ $Cs_4M(II)Sb_2Cl_{12}$ NCs (M = Mn, Cd)	Trigonal ($R\bar{3}m$)	Hot injection method	∼3.17 eV 619–640 nm	Photodetector (responsivity 0.98×10^4 A W^{-1})	55
Gray *et al.* (2021)	$Cs_4CdBi_2Cl_{12-z}X_z$, MCs (X = Br, I)	Trigonal ($R\bar{3}m$)	Acid precipitation	3.20 to 2.99 eV	X-site tuning	56
Aramel *et al.* (2022)	$Cs_4CuBi_2Br_{12}$	Monoclinic ($C2/m$)	Spin coating	2.59 eV	Compositional tuning	57
	$Cs_4MnBi_2Br_{12}$ Thin films	Trigonal ($R\bar{3}m$)		2.52 eV		
Yang *et al.* (2022)	$Cs_4MnBi_2Cl_{12}$ $Cs_4CdBi_2Cl_{12}$ NCs	Trigonal ($R\bar{3}m$)	Hot injection method	3.38–3.42 eV 614 nm		58
Li *et al.* (2022)	Ln^{3+} doped $Cs_4MnBi_2Cl_{12}$ MCs	Trigonal ($R\bar{3}m$)	Acid precipitation	580 nm 980 nm 1540 nm	Anticounterfeiting NIR emission	59
Lin *et al.* (2022)	$Cs_4Cd_xMn_{1-x}Bi_2Cl_{12}$:$RE^{3+}$ (Ho, Er, Tm, Nd) SCs	Trigonal ($R\bar{3}m$)	Hydrothermal	985 nm 1194 nm 1488 nm	LED NIR emission	60
Liu *et al.* (2023)	$Cs_4MnSb_2Cl_{12}$ $Cs_{10}MnSb_6Cl_{30}$ SCs	Orthorhombic ($Pnnm$)	Hydrothermal & solid-state synthesis	2.98 eV 620 nm	Reduced dimensionality (enhanced PL)	61
Zhao *et al.* (2023)	$Cs_4Cd_{1-x}Mn_xBi_2Cl_{12}$ MCs	Trigonal ($R\bar{3}m$)	Co-precipitation method	600 nm	Suppressed Mn-Mn coupling	62
Wang *et al.* (2023)	$Cs_4MnBi_2Cl_{12}$ nanoplates	Trigonal ($R\bar{3}m$)	Hot injection method	580–600 nm	X-ray scintillators	63
Dang *et al.* (2023)	$Cs_4Cd_{1-x}Mn_xBi_2Cl_{12}$:$RE^{3+}$ (RE: Nd, Ho, Er, Tm) SCs	Trigonal ($R\bar{3}m$)	Hydrothermal method	520–1650 nm	White LED	64
Liu *et al.* (2023)	$Cs_3Bi_2Cl_9$ $Cs_4MnBi_2Cl_{12}$ MCs	Trigonal ($R\bar{3}m$)	Acid precipitation	3.0 eV 3.1 eV ∼615 nm	Mechanism of Mn^{2+} induced luminescence	65
Wei *et al.* (2023)	$Cs_4Mn(Bi_{1-x}Sb_x)_2Cl_{12}$ MCs	Trigonal ($R\bar{3}m$)	Acid precipitation	3.10–2.81 eV 520–780 nm	Photocatalytic CO_2 reduction	66
Chen *et al.* (2024)	$Cs_4CdBi_2Cl_{12}$: Ag^+ MCs	Trigonal ($R\bar{3}m$)	Hydrothermal method	2.95–2.57 eV 540–660 nm	White LED	67
Gao *et al.* (2024)	$Cs_4Mn_{1-x}Cu_xSb_2Cl_{12}$ MCs	Trigonal ($R\bar{3}m$)	Acid precipitation	2.98–1.68 eV	Photocatalytic CO_2 reduction (CO yield of 503.86 μmol g^{-1} after 3 h of irradiation)	68
Singh *et al.* (2025)	$Cs_4MnBi_2Cl_{12}$ MCs	Trigonal ($R\bar{3}m$)	Acid precipitation	605 nm	Anticounterfeiting	69
Huang *et al.* (2025)	$Cs_4Mn(Co_xBi_{1-x})_2Cl_{12}$ MCs	Trigonal ($R\bar{3}m$)	Acid precipitation	2.76 eV 2.82 eV	Photocatalytic CO_2 reduction (a CO yield of 69.16 μmol g^{-1} h^{-1})	70
Chen *et al.* (2025)	$Cs_4CdBi_2Cl_{12}$ MCs	Trigonal ($R\bar{3}m$)	Acid precipitation	603 nm 670 nm	Photocatalytic CO_2 reduction (a CO yield of 90.77 after 3 h of irradiation)	71
Liu Y *et al.* (2025)	$Cs_4Cd_{0.8}Cu_{0.2}Bi_2Cl_{12}$ MCs	Trigonal ($R\bar{3}m$)	Acid precipitation	2.17 eV	Photocatalytic CO_2 reduction (a CH_4 yield of 8.78 μmol g^{-1} 3 h^{-1})	72
Mai *et al.* (2023)	$Cs_4ZnSb_2Cl_{12}$ NCs	Monoclinic ($C2/m$)	Hot injection method	Absorption from 400 to 650 nm	Photocatalytic toluene oxidation	73
Liu J *et al.* (2025)	$Cs_4ZnBi_2Br_{12}$ NCs	Monoclinic ($C2/m$)	Water-oil biphasic method		Anion exchange	74
Liu *et al.* (2022)	$Cs_4CuIn_2Cl_{12}$ NCs	Monoclinic ($C2/m$)	Moisture assisted hot injection method	3.56 eV 381 nm	Moisture assisted PL enhancement	75
Liu *et al.* (2024)	$Cs_4CuIn_2Cl_{12}$ NCs $Cs_4ZnIn_2Cl_{12}$ NCs $Cs_4CoIn_2Cl_{12}$ NCs	Monoclinic ($C2/m$)	Hot injection method	3.60 eV/380 nm 3.74 eV/416 nm 3.63 eV/430 nm	Enhancement of PLQY (0.12–11.4%)	76
Yukta *et al.* (2025)	$Cs_4CoSb_2Cl_{12}$ NCs $Cs_4CoBi_2Cl_{12}$ NCs $Cs_4CoIn_2Cl_{12}$ NCs		Hot injection method	2.88 eV/416 nm 3.23 eV/419 nm 3.67 eV/403 nm	Photoelectrochemical activity	77

charge carrier dynamics of the material. Since the divalent cation plays a direct role in the formation of metal halide octahedra, substitution at this position considerably alters orbital hybridization with halide ligands, modifies lattice distortion and influences exciton localization. Hence, B(II)-site engineering is a viable technique for optimizing the band gap, photoluminescence behaviour, defect tolerance, and structural stability of lead-free LDPs.

Among the various compositions reported, $Cs_4CuSb_2Cl_{12}$ represents one of the earliest and most widely investigated LDP systems. This compound can be viewed as originating from the layered structure $Cs_3Sb_2Cl_9$ through the insertion of divalent cations (Cu^{2+}), forming a vacancy-ordered layered double perovskite framework.[88] The inclusion of copper introduces Cu-3d electronic states that strongly hybridise with Cl-p and Sb-p orbitals, resulting in a significant lowering of the band gap and improved visible-light absorption.[25] Both theoretical and experimental findings demonstrate that even a small amount of Cu^{2+} can drastically alter the band structure, emphasising the great sensitivity of LDP electronic properties to B-site composition.[45] Systematic substitution of different metal ions at this position provides additional control over structural dimensionality, optical transitions and charge carrier transport behaviour. This section discusses the impacts of different cationic substitutions on the structure and properties of LDPs.

2.2.1 Effect of Cu^{2+}.

The presence of partially filled Cu-3d orbitals makes copper substitution one of the more effective ways for band gap engineering in LDPs. These orbitals introduce new electronic states near the band boundaries and improve hybridisation with halide p-orbitals, reducing the band gap and enhancing optical absorption in the visible region.

A clear example of this behaviour is observed in the $Cs_4Mn_{1-x}Cu_xSb_2Cl_{12}$ series, where the bandgap can be continuously tuned from $\sim$3.0 eV for the Mn-rich compound to nearly 1.0 eV with increasing Cu content (Fig. 2(a)). Notably, even a small amount of copper inclusion ($x = 0.1$) leads to a significant reduction in the band gap from 3.0 eV to 1.7 eV, indicating a strong perturbation of the electronic structure.[24,68] Similar band gap narrowing was seen in $Cs_4Cu_{1-x}Cd_xSb_2Cl_{12}$, where Cu substitution results in a pronounced red shift in the absorption spectrum (Fig. 2(b)).[32] Copper substitution also causes structural and electronic changes in certain LDP systems. In the $Cs_4Cu_xAg_{2-2x}Sb_2Cl_{12}$ series, gradual substitution of Ag^+ by Cu^{2+} triggers the structural transformation from the cubic double perovskite phase ($Cs_2AgSbCl_6$) to a monoclinic layered double perovskite phase ($Cs_4CuSb_2Cl_{12}$). This transition is accompanied by a shift from an indirect to a direct band gap, substantially improving light absorption efficiency.[89]

Despite its significant impact on band gap modulation, Cu^{2+} generally does not serve as an efficient luminescent centre in many LDP systems. When compared to Mn-rich analogues, Cu-containing compositions in the $Cs_4Mn_{1-x}Cu_xSb_2Cl_{12}$ system exhibit weak photoluminescence.[68] This behaviour suggests that copper primarily modifies the band structure rather than serving as a radiative recombination centre. In contrast, a copper-containing lead-free perovskite $Cs_3Cu_2X_5$ (X = Cl, Br) shows excellent emission property, with photoluminescence quantum yield (PLQY) near unity.[92]

The underlying mechanism for these changes originates from the introduction of Cu-3d electronic states within the band structure. These states may create mid gap levels or directly contribute to the valence band maximum, thereby reducing the band gap. Furthermore, the significant Jahn–Teller distortion associated with Cu^{2+} can alter octahedral symmetry, impacting both carrier localization and structural stability.[32,68] Overall, copper substitution is a viable method for increasing visible-light absorption and tuning the electrical characteristics of LDPs.

2.2.2 Effect of Mn^{2+}.

Unlike copper, manganese substitution is primarily associated with luminescence behaviour in layered double perovskites. Mn^{2+} ions introduce characteristic spin and parity forbidden d–d transitions that produce orange-red photoluminescence, making Mn- based LDPs attractive for light-emitting applications.

Mn incorporation can also trigger structural transformations. For instance, gradual substitution of Mn^{2+} in the $Cs_3Bi_2Cl_9$ system leads to a phase transition from an orthorhombic structure to the trigonal $Cs_4MnBi_2Cl_{12}$ layered double perovskite. This structural evolution arises from the smaller ionic radius of Mn^{2+} compared with Bi^{3+}, which induces lattice contraction and shifts PXRD peaks toward higher diffraction angles. The structural transition also reflects a dimensional transformation from a one-dimensional framework to a two-dimensional layered structure.[65]

$Cs_4MnBi_2Cl_{12}$ and $Cs_4MnSb_2Cl_{12}$ exhibit distinct photoluminescence behaviours and PLQYs. $Cs_4MnBi_2Cl_{12}$ typically displays strong orange-red emission centred around 605–619 nm. Its PLQY strongly depends on the materials' morphology: single crystals can reach PLQY values of approximately 25.7%, whereas microcrystals exhibit lower PLQY values of around 7.8–12.1% due to increased trap states and grain boundaries.[91] Temperature-dependent photoluminescence studies further reveal that the emission intensity decreases with increasing temperature, indicating thermally activated non-radiative recombination mediated by electron–phonon coupling.[91] Nanocrystals of pure $Cs_4MnBi_2Cl_{12}$ generally exhibit very low PLQY ($<1\%$), which is mainly attributed to the surface defects and enhanced non-radiative recombination pathways. However, alloying with Cd^{2+} has been reported to significantly enhance the PLQY by suppressing non-radiative decay channels and improving energy transfer to the Mn^{2+} emission centre (Fig. 2(f)).[55,69]

A significant enhancement of photoluminescence has been observed in Mn-doped single crystals of the $Cs_4CdBi_2Cl_{12}$ system. Dilute Mn alloying produces intense orange emission with photoluminescence quantum yields reaching $\sim$57% (Fig. (2e)).[50] The high luminescence efficiency arises because the Cd-rich host lattice spatially isolates Mn^{2+} centres, thereby suppressing Mn–Mn interactions that typically promote non-radiative energy transfer. This comparison of Mn-rich and Cd-rich compositions demonstrates an important design principle:

efficient emission occurs when Mn^{2+} ions remain sufficiently isolated within the wide-bandgap host lattice.[62,63,93]

In contrast, $Cs_4MnSb_2Cl_{12}$ exhibits relatively weak red photoluminescence at room temperature. The emission is typically red shifted compared with $Cs_4MnBi_2Cl_{12}$, appearing near ∼640 nm, and is characterised by a broader full width at half maximum of ∼105 nm. Reported PLQY values for pure $Cs_4MnSb_2Cl_{12}$ are generally lower than those of the Bi-based analogue, reflecting less efficient energy transfer to the Mn^{2+} emission centre.[94] Nevertheless, alloyed compositions such as $Cs_4Mn_{1-x}Cd_xSb_2Cl_{12}$ show improved photoluminescence efficiency, demonstrating that compositional engineering can partially overcome the intrinsic limitations of the Sb-based system.[95,96]

The presence of Mn^{2+} can introduce impurity energy levels within the band gap, influencing the material's electronic structure and optical characteristics. This substitution can alter charge carrier dynamics by introducing trapping states. For instance, in $Cs_4MnSb_2Cl_{12}$ nanocrystals, Mn^{2+} contributes to ultrafast components attributed to carrier trapping, which competes with energy transfer processes and can reduce the photoluminescence quantum yield.[55,69] The presence of Mn^{2+} influences the electronic structure by contributing to the valence and conduction band edges, facilitating energy transfer processes and potentially altering carrier mobility (Fig. 2(g) and (h)).[69,91] While Mn^{2+} doping can enhance optical properties, excessive concentrations might lead to Mn–Mn coupling, which can weaken radiative recombination and decrease PLQY. The detailed mechanism suggests that while Bi^{3+} in $Cs_4MnSb_2Cl_{12}$ acts as a sensitiser, Mn^{2+} contributes to the emission through d–d transitions.[69] These effects highlight the critical role of Mn^{2+} in modulating defect states and charge carrier behaviour within these perovskite structures, impacting their luminescence and potentially optoelectronic performance.

2.2.3 Effect of Zn^{2+}.

Zinc substitution offers a different strategy for tuning the electronic structure of LDPs. In contrast to Cu^{2+} and Mn^{2+}, Zn^{2+} possesses a filled d^{10} electronic configuration, meaning that its influence on the band structure mainly arises from Zn-4s orbital contributions to the conduction band.

In $Cs_4ZnSb_2Cl_{12}$, Zn-4s orbitals dominate the conduction band edge, resulting in a narrow direct band gap and a reduced electron effective mass. In contrast, Cu-containing systems typically exhibit highly localised Cu-3d states near the band edges, which can limit carrier mobility. Consequently, Zn-based LDPs are expected to exhibit improved carrier transport properties, making them attractive for optoelectronic and photocatalytic applications.[90]

Additionally, nanocrystal forms of $Cs_4ZnSb_2Cl_{12}$ display size-dependent bandgap tuning due to quantum confinement effects (Fig. 2(c)), which is reflected in the visible colour change of the nanocrystal solution (Fig. 2(d)). As the nanocrystal size decreases, the confinement energy increases, leading to

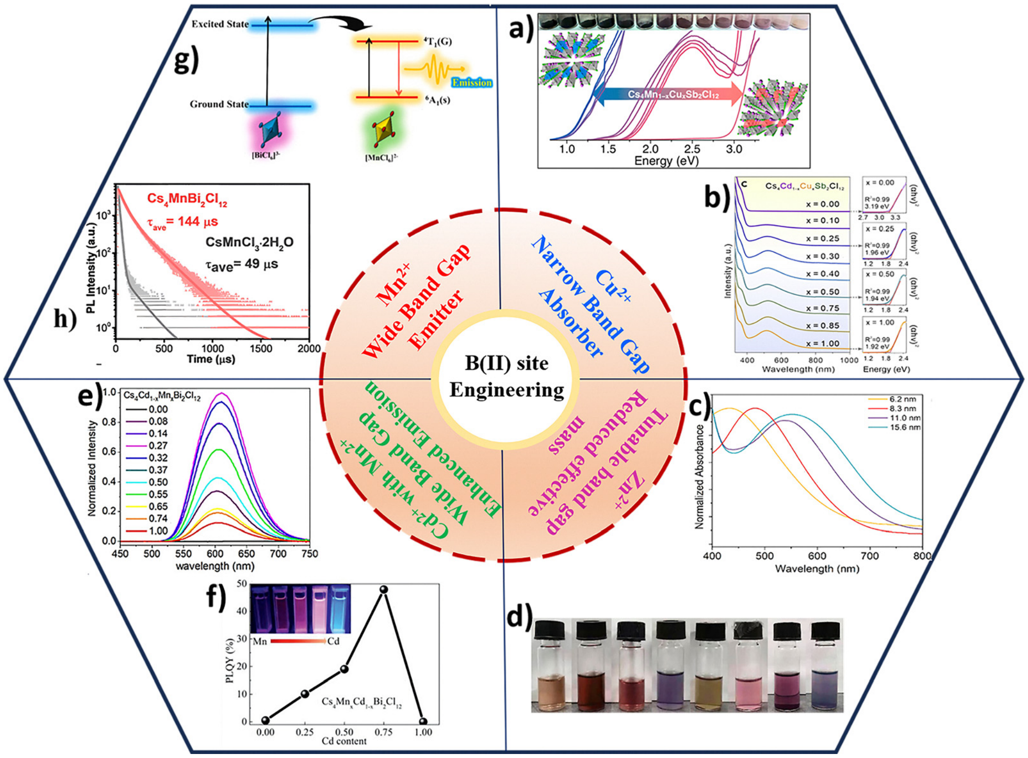

Fig. 2 Schematic showing the influence of B(II) site cations on optoelectronic properties of LDPs. Copper doping induced band gap modulation in $Cs_4Mn_{1-x}Cu_xSb_2Cl_{12}$ (a)[24] and $Cs_4Cd_{1-x}Cu_xSb_2Cl_{12}$ (b).[32] Tunable band gap in $Cs_4ZnSb_2Cl_{12}$ NCs with precise control over shape and size (c) and (d).[90] Enhanced emission and photoluminescence quantum yield in Cd^{2+} incorporated $Cs_4Mn_xCd_{1-x}Bi_2Cl_{12}$ NCs (e) and (f).[50,55] Emission mechanism and increased carrier lifetime of $C_4MnBi_2Cl_{12}$ (g) and (h).[69,91] Reprinted with permission from ref. 24, 32, 50, 55, 69, 91, and 90.

widening of the band gap. Strong confinement effects are observed when particle size approaches approximately 9–10 nm, demonstrating that combining B-site engineering with nanoscale control provides additional flexibility for tailoring optoelectronic behaviour.[90]

Despite the promising characteristics, Zn-based LDPs remain relatively unexplored. Only a limited number of studies have reported Zn-containing compositions, and even for compounds such as $Cs_4ZnBi_2Br_{12}$.[74] Systematic investigations of their structural, optical and electronic properties are still scarce. This highlights the need for further experimental and theoretical studies to fully understand and exploit the potential of Zn-based LDP systems.

2.2.4 Effect of monovalent cation substitution. In addition to divalent metals, partial substitution with monovalent cations such as Ag^+ and Na^+ can further modify the structural and optical properties of LDPs. These substitutions influence lattice parameters, crystal structure and electronic band structures, thereby providing another pathway for band gap and photoluminescence tuning.

In the $Cs_4Cu_xAg_{2-2x}Sb_2Cl_{12}$ system, increasing copper content gradually converts the structure from a cubic double perovskite to a monoclinic layered double perovskite. This structural transition is accompanied by the emergence of strong visible absorption and a change from an indirect to a direct band gap, illustrating the close relationship between crystal symmetry and electronic band structure.[89]

Similarly, Ag^+ doping in $Cs_4CdBi_2Cl_{12}$ significantly enhances photoluminescence intensity, with the maximum emission observed at low doping concentrations (~0.8%). The absorption position was gradually red shifted by increasing the Ag^+ doping concentration. The decrease in band gap was observed from 2.95 to 2.57 when the doping quantity is 5.0%.[67]

Na^+ alloying introduces additional structural effects due to its relatively larger ionic radius. In $Cs_4MnBi_2Cl_{12}$, Na substitution expands the lattice and elongates Mn–Cl bonds, which decreases crystal-field splitting around Mn^{2+} centres. As a result, the energy of the Mn d–d transition increases, leading to a blue shift in photoluminescence (PL) emission. As the Na^+ content grows, the PL peak moves continually. For example, the Na-doped sample $Cs_4Mn_{0.5}NaBi_2Cl_{12}$ exhibits a PL peak at 590 nm, and further Na^+ incorporation continues the blue-shift trend.[55]

Monovalent substitution in LDPs generally occurs through a heterovalent alloying mechanism that maintains overall charge neutrality while perturbing the metal halide framework. Incorporation of cations such as Ag^+ or Na^+ alters lattice parameters, metal halide bond lengths and octahedral distortions, which in turn influence the electronic band structure. In particular, d^{10} cations like Ag^+ can contribute s or d orbital character near the band edges, modifying the band dispersion and band gap energies, whereas alkali metals such as Na^+ mainly affect the electronic structure indirectly through lattice expansion and changes in crystal field environments. These structural and electronic perturbations collectively provide a mechanistic basis for tuning the optoelectronic properties of LDPs through monovalent cation substitution.

Arramel *et al.* (2022) reported several new LDPs, including $Cs_4M(\text{II})Bi_2Br_{12}$ (M(II) = Cu, Mn, Pb, Sr).[57] However, a subsequent re-evaluation using first principles thermodynamic analysis and simulated X-ray diffraction patterns suggested that these compounds are thermodynamically unstable and may preferentially decompose into the $Cs_3Bi_2Br_9$ phase. The study further indicated that the experimental XRD patterns and nearly identical band gap values (~2.6 eV) reported for different M(II) cations are consistent with $Cs_3Bi_2Br_9$ rather than the proposed layered double perovskite structures.[97] This highlights the importance of rigorous structural verification when reporting new LDP phases.

Comparative analysis of B(II) site substitution studies reveals several design principles for the rational development of LDPs. Transition metals with partially filled d orbitals, such as Cu^{2+}, introduce localised 3d states that enable substantial band gap tuning and improved visible light absorption. Incorporation of dilute luminescent centres, particularly Mn^{2+}, can significantly enhance photoluminescence efficiency by suppressing concentration quenching in a wide band gap host lattice. In contrast, closed-shell d^{10} cations like Zn^{2+} contribute s-orbital character to the conduction band, which can lower the electron effective mass and promote improved charge transport. Additionally, lattice distortions arising from Jahn–Teller effects or ionic size mismatches influence octahedral symmetry, thereby affecting exciton localisation and defect tolerance. Finally, compositional alloying at the B-site provides a strategy to stabilise layered frameworks while simultaneously tuning optical and electronic properties. Collectively, these insights highlight B(II)-site engineering as a powerful approach for tailoring the structural and optoelectronic characteristics of lead-free LDPs for optoelectronic and energy conversion applications.

2.3 B(III) site engineering

The B(III) site is generally occupied by trivalent metal cations such as antimony(III) and bismuth(III), which strongly influence the electronic band structure of LDPs. These cations contribute significantly to the conduction band and valence band characteristics due to their ns^2 lone-pair electronic configuration. As a result, modification of the B(III) site can affect band gap energies, optical absorption behaviour and exciton localisation. Substitution between Sb^{3+} and Bi^{3+} or substitution or alloying with other trivalent metals provides an effective route to tailor the optoelectronic properties of these materials.

2.3.1 Effect of antimony and bismuth on LDPs. The presence of antimony or bismuth in quadruple-perovskites influences their optoelectronic properties, particularly their absorption and photoluminescence behaviour. For instance, $Cs_4CdSb_2Cl_{12}$ NCs exhibit a wide-bandgap absorption spectrum with a small peak around 370 nm. When Bi^{3+} is present, such as in $Cs_4CdBi_2Cl_{12}$ and $Cs_4MnBi_2Cl_{12}$ NCs, an additional strong absorption peak appears around 330 nm, which is attributed to the $^1S_0 \rightarrow {}^3P_1$ transition of Bi^{3+} ions. Cd-based NCs containing either Sb or Bi show photoluminescence at lower temperatures (200 K) but not at room temperature. The inclusion of Bi can alter the PL peak position: for example, in $Cs_4MnBi_xSb_{2-x}Cl_{12}$ NCs, the PL spectra gradually red-shift as the Sb^{3+} content increases, indicating that alloying with Sb^{3+} influences the local structure around Mn^{2+} and thus the optical properties. This suggests that the presence and ratio of Sb^{3+} and Bi^{3+} play a role in tuning the electronic band structure and emission characteristics of these LDP NCs.[55] Moreover, substituting Sb^{3+} with Bi^{3+} has a substantial influence on charge carrier dynamics. $Cs_4CdBi_2Cl_{12}$ demonstrates reduced carrier recombination, as indicated by its lower PL intensity and shorter average carrier lifetime compared to $Cs_4CdSb_2Cl_{12}$. This suppression of recombination is accompanied by an increase in photocurrent density and a decrease in charge transfer resistance, reflecting more efficient charge separation and hence improved photocatalytic CO yield.[71] The compound containing fixed amount of Mn^{2+} and Cd^{2+} with varying amount of Sb^{3+} and Bi^{3+}, that is, $Cs_4Cd_{0.8}Mn_{0.2}(Sb_{1-z}Bi_z)_2Cl_{12}$ exhibited decreased emission efficiency with increase in Sb^{3+} concentration (Fig. 3(g)).[98] These findings spotlight the critical role of trivalent metal cation selection in tuning the optoelectronic properties of LDPs for photocatalytic applications.

Sb^{3+} alloying in $Cs_4Mn(Bi_{1-x}Sb_x)_2Cl_{12}$ LDPs improves charge transfer efficiency by limiting unwanted relaxation of photogenerated electrons and reducing radiative recombination. Sb^{3+} incorporation suppresses electron transfer to $[MnCl_6]^{4-}$ emission centres, leading to weaker PL but better photocatalytic performance (Fig. 3(h)). Time-resolved PL measurements confirm this effect by showing faster PL decay and shorter lifetimes after Sb^{3+} doping. In Sb-alloyed samples, increasing Sb^{3+} content causes the light absorption edge to shift from 400 nm to around 460 nm, enhancing light-harvesting capability. The absorption edge reaches its maximum at a Bi : Sb atomic ratio of 2 : 3, which also corresponds to a visible colour change from white ($Cs_4MnBi_2Cl_{12}$) to yellow ($Cs_4Mn(Bi_{0.4}Sb_{0.6})_2Cl_{12}$). Based on Tauc plots, the bandgap (E_g) of $Cs_4Mn(Bi_{1-x}Sb_x)_2Cl_{12}$ samples decreases with higher Sb^{3+} content, reaching its lowest value 2.81 eV when $x = 0.6$.[66]

By varying '*n*' in the general formula, $A(\square_n B'_{1-3n} B_{2n})X_3$ (where *n* denotes the non-stoichiometric concentration of vacancies relative to a single ABX_3 perovskite formula unit), a series of novel compounds exhibiting different octahedral connectivity can be obtained. B-site-deficient halide perovskites, such as the layered perovskite $A_3B_2X_9$ and the layered double perovskite $A_4B(\text{II})B(\text{III})_2X_{12}$, are formed when *n* equals 0.33 and 0.25, respectively. Recently, Liu *et al.* (2023) reported a novel 10-layer hexagonal perovskite, $Cs_{10}MnSb_6Cl_{30}$, which features 30% B-site vacancies ordered at both face-sharing and corner-sharing sites. This compound was synthesised using straightforward methods, including the hydrothermal method for growing single crystals and solid-state synthesis for obtaining the powder sample. The resulting one-dimensional perovskite structure exhibits enhanced photoluminescence and improved photoluminescence quantum yield compared to the two-dimensional $Cs_4MnSb_2Cl_{12}$, which has 25% vacancy ordering.[61]

2.3.2 Indium-based LDPs. Indium is a vital component in lead-free $Cs_4CuIn_2Cl_{12}$ double perovskite nanocrystals (NCs), playing a key role in enhancing their optoelectronic properties, especially in the ultraviolet (UV) region. Replacing the Sb^{3+} ion in $Cs_4CuSb_2Cl_{12}$ with the less toxic In^{3+} not only reduces environmental concerns but also enables compositional tuning for improved optical response. The bandgap of $Cs_4CuIn_2Cl_{12}$ NCs (3.56–3.82 eV) is significantly wider than that of $Cs_4CuSb_2Cl_{12}$ (1.0–1.8 eV), primarily due to the introduction of additional valence band states from copper and chlorine. The valence band is predominantly formed by Cu and Cl orbitals, and the overall electronic structure is defined by the interaction among In, Cu, and Cl. These interactions, which are sensitive to synthesis conditions, dictate the material's optical absorption and emission behaviour (Fig. 3(c)), ultimately influencing the optoelectronic performance of $Cs_4CuIn_2Cl_{12}$ nanocrystals.[75]

The doping of In^{3+} with a relatively small ionic radius in the $Cs_4Mn(Bi_{1-x}In_x)_2Cl_{12}$ is bound to alter the internal structure. When In^{3+} is introduced, it causes distortion in the octahedron and the crystal field strength of the Mn^{2+} ion changes, resulting in the gradual red shift of the emission band from 606 nm to 616 nm (Fig. 3(d)). The large difference in the ionic radii of In^{3+} and Bi^{3+} limits the doping content of In^{3+} to 12%, while the excessive doping leads to the appearance of other phases and causes structural instability.[53]

Substitution at the B(II) site also strongly affects the photoluminescence behaviour of $Cs_4CuIn_2Cl_{12}$ nanocrystals. Replacing Cu^{2+} with Co^{2+} or Zn^{2+} introduces greater lattice distortion, which promotes the formation of self-trapped excitons (STEs).[100] These excitons act as efficient radiative recombination centres, leading to enhanced photoluminescence quantum yields. Consequently, $Cs_4CoIn_2Cl_{12}$ and $Cs_4ZnIn_2Cl_{12}$ nanocrystals exhibit PLQYs of 4.3% and 11.4%, respectively, whereas pristine $Cs_4CuIn_2Cl_{12}$ remains nearly non-emissive with a PLQY of only 0.12%.

2.3.3 Effect of M(III) cations (In^{3+}, Bi^{3+}, or Sb^{3+}) in $Cs_4CoM(III)_2Cl_{12}$. Furthermore, substituting the M(III) cation (In^{3+}, Bi^{3+}, or Sb^{3+}) in $Cs_4CoM(\text{III})_2Cl_{12}$ nanocrystals significantly influences their optical properties. As the M(III) cation changes progressively from In^{3+} to Bi^{3+} and then to Sb^{3+}, the bandgap energy decreases systematically from 3.67 eV ($Cs_4CoIn_2Cl_{12}$) to 3.23 eV ($Cs_4CoBi_2Cl_{12}$) and further to 2.88 eV ($Cs_4CoSb_2Cl_{12}$). This reduction is primarily attributed to increased spin–orbit coupling and alterations in the electronic structure induced by the different trivalent metal ions. The colour of the NCs changes from turquoise blue (In^{3+}) to light blue (Bi^{3+}) and finally to dark green (Sb^{3+}), correlating with the observed reduction in bandgap. Changes in the absorption spectra also reflect this substitution. $Cs_4CoSb_2Cl_{12}$ exhibits two excitonic peaks between 300 and 450 nm along with a broad absorption band from 600 to 720 nm, attributed to $[CoCl_4]^{2-}$ tetrahedral species. This broad band is absent in the Bi-containing variant, suggesting that the ligand field environment and electronic interactions are strongly influenced by the identity of the trivalent metal cation. The Bi-based compound showed strong photo-response and improved photocurrent output.[77]

2.3.4 Transition metal incorporation at the M(III) site. Cobalt doping in $Cs_4MnBi_2Cl_{12}$ modifies its electronic structure by inducing spin polarisation, which enhances carrier

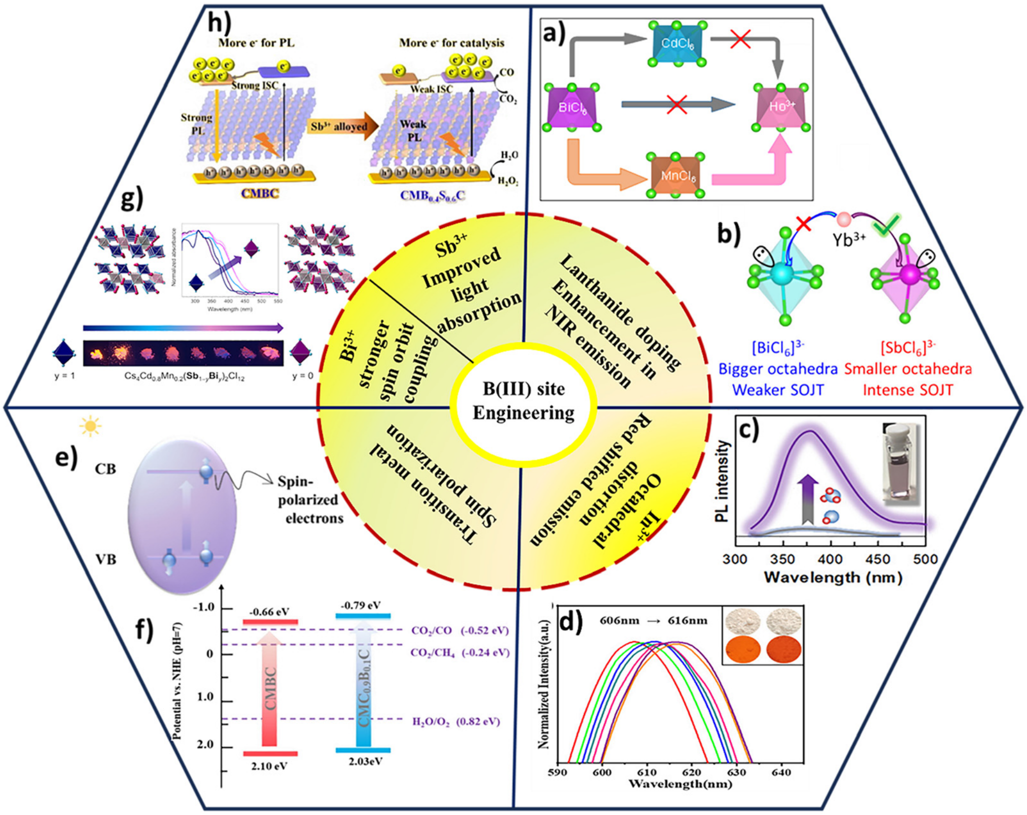

Fig. 3 B(III) site tuning in LDPs. Energy transfer in Ho^{3+} doped Cs$_4$MnBi$_2$Cl$_{12}$ (a).[64] Higher lanthanide doping efficiency in smaller octahedra of Sb^{3+}, induced by intense second order John teller distortion. (b)[99] Moisture assisted PL enhancement in Cs$_4$CuIn$_2$Cl$_{12}$. (c)[75] Red shift in the emission spectra of Cs$_4$MnBi$_2$Cl$_{12}$ with increasing In^{3+} content (d).[53] Band alignment diagram and electron spin polarization suppressed recombination in Cs$_4$MnCo$_{0.9}$Bi$_{0.1}$Cl$_{12}$ (e) and (f).[70] Effect of Bi^{3+} and Sb^{3+} substitution on photoluminescence efficiency of Cs$_4$Cd$_{0.8}$Mn$_{0.2}$(Sb$_{1-y}$Bi$_y$)$_2$Cl$_{12}$ (g).[98] Suppression of fluorescence emission in Sb^{3+} alloyed Cs$_4$MnBi$_2$Cl$_{12}$ (h).[66] Reprinted, with permission, from ref. 98, 66, 75, 53, 70, 99, and 64.

separation and prolongs carrier lifetimes. Theoretical studies show that Co^{2+} doping increases spin-polarised photoexcited carriers, generating an internal electric field that promotes charge separation and transport. This spin polarisation results from the hybridisation of cobalt 3d orbitals with the host lattice and lattice distortion, leading to asymmetric charge distribution (Fig. 3(f)). Compared to pure CMBC, which has an absorption edge around 480 nm, Co-doped samples showed an additional absorption peak in the 600–750 nm range, indicating improved red and near-infrared light capture due to Co^{2+} doping. Tauc plots from UV-Vis DRS data showed a slight increase in band gap from 2.76 eV (Cs$_4$MnBi$_2$Cl$_{12}$) to 2.82 eV (Cs$_4$MnCo$_{0.9}$Bi$_{0.1}$Cl$_{12}$) (Fig. 3(e)). This enhanced visible-light absorption is mainly due to changes in the electronic structure and spin polarisation, rather than a direct band gap reduction. Overall, Co^{2+} doping improves photocatalytic performance by enhancing carrier dynamics and spin effects.[70]

2.3.5 Lanthanide doping-induced enhancement in NIR emission. To enhance the optoelectronic properties of the lead-free perovskites, lanthanide ion doping is one of the effective and promising paths. To study the effect of Ln^{3+} doping in lead-free LDPs, Lin *et al.* have synthesised a series of Ln^{3+}(Yb^{3+}, Er^{3+} and Nd^{3+}) doped lead-free perovskites, including vacancy-induced layered perovskites, double perovskites and layered double perovskites. Ln^{3+}-doped lead-free perovskites exhibited near-infrared (NIR) emissions, originating from the characteristic f-f transitions of the incorporated lanthanide ions. Increasing Sb^{3+} incorporation into Sb^{3+}/Bi^{3+} alloyed perovskites leads to enhanced NIR emission and allows for higher Ln^{3+} doping concentrations. Despite the size mismatch between Sb^{3+} and Ln^{3+}, even large ions like Nd^{3+} show high doping efficiency in Sb^{3+}-based perovskite NCs. This is attributed to the high polarizability of Ln^{3+} ions, enabling better accommodation at B(III) sites and enhancing structural stability. The strong second-order Jahn–Teller distortion in [SbCl$_6$]$^{3-}$ octahedra may also contribute to this improved doping efficiency (Fig. 3(b)).[99] The incorporation of lanthanides (Ln =Yb, Er, Nd) in the quadruple perovskite Cs$_4$MnBi$_2$Cl$_{12}$ gives orange-red emission from the d–d transition of Mn^{2+}. The multimodal emission of the rare earth metals enables the tailoring of the emission properties to achieve the desired applications.[59]

Furthermore, to achieve interesting optical properties in visible and near-infrared regions, researchers have successfully incorporated the rare-earth ion doping strategy. By using the hydrothermal method, a series of rare earth ion-doped Cs$_4$Mn$_{1-x}$Cd$_x$Bi$_2$Cl$_{12}$ were synthesised. Cs$_4$MnBi$_2$Cl$_{12}$ has an indirect narrow bandgap at 2.72 eV and a large absorption with a direct bandgap at 3 eV. By the introduction of Cd^{2+}, the conversion from the indirect to the direct band gap is observed. Furthermore, RE^{3+} doping can increase the photoluminescence quantum yield to 35–59% due to the superposition of additional RE^{3+} emissions. The rare-earth ion-doped $Cs_4MnBi_2Cl_{12}$ is useful in white light-emitting LED applications.[60]

Rare-earth (RE^{3+}) ions have abundant 4f states that enable sharp, distinct red and NIR emissions. When doped into $Cs4Cd_{1-x}Mn_xBi_2Cl_{12}$ vacancy-ordered quadruple perovskites, their luminescence is significantly enhanced by Mn^{2+}, which acts as an energy transfer bridge. As Mn^{2+} gradually replaces Cd^{2+}, the RE^{3+} photoluminescence in the red and NIR regions intensifies, peaking at full Mn substitution. In contrast, RE^{3+} ions in $Cs_4CdBi_2Cl_{12}$ without Mn^{2+} show no red-NIR emission, highlighting the key role of Mn^{2+} (Fig. 3(a)). Co-doping RE^{3+} into $Cs_4MnBi_2Cl_{12}$ extends emission into both NIR-I and NIR-II ranges, making it promising for NIR detection applications.[64]

Collectively, the studies discussed above demonstrate that the identity of the trivalent metal cation plays a decisive role in determining the structural stability and optoelectronic behaviour of LDPs. Comparative studies reveal that compounds containing the Bi^{3+} cation generally exhibit superior spin–orbit coupling and enhanced charge transport compared to those incorporating the Sb^{3+} cation, which may absorb light more effectively and modulate their band gaps *via* alloying. Incorporation of the In^{3+} cation results in wider band gap materials and potentials for ultraviolet optoelectronic applications. Additionally, the incorporation of lanthanide ions leads to enhanced NIR emission for lighting applications. These observations highlight several emerging design principles: Specifically, tuning the B(III) site composition allows for systematic tuning of the band gap through optimisation of orbital interactions and spin–orbit coupling. Furthermore, alloying or hetero-valent doping is found to improve defect tolerance and suppress recombination. Additionally, cation design can be used to improve structural stability by tuning octahedral distortion and lattice strain. Therefore, rational engineering of the B(III) site provides a powerful strategy to optimise the electronic structure, defect chemistry, and optical performance of LDPs, guiding the development of stable and efficient lead-free perovskite materials for advanced applications.

Simultaneous engineering of both B(II) and B(III) sites provides a broader compositional space for tuning the structural and electronic properties of LDPs. Modifications at either metal site can influence octahedral connectivity, band structure, and charge carrier dynamics. Consequently, combined B-site engineering offers a powerful strategy for optimising stability, band gap and photophysical behaviour in LDPs.

2.4 X-site

The X-site anions in most of the previously reported studies are chlorides. However, the strong electronegativity and small ionic radius of Cl^- typically lead to relatively wide band gaps, thereby limiting optical tunability. Consequently, partial substitution of chloride with heavier halides such as Br^- and I^- has emerged as an effective strategy for modulating the electronic structure and optical absorption of $Cs_4B(II)B(III)_2Cl_{12}$ compounds.

Systematic halide substitution studies reveal that the overall vacancy-ordered quadruple perovskite framework with $R\bar{3}m$ symmetry is generally preserved upon partial replacement of Cl^- with Br^- or I^-. In Cd^{2+}-containing systems, significant bromide incorporation (>25%) can be achieved without disrupting the host lattice. The larger Br^- and I^- anions preferentially occupy sites adjacent to the cation-vacancy layers, indicating that local structural flexibility around the vacancy planes facilitates halide substitution. Notably, $Cs_4CdM(III)_2Cl_{12}$ compounds exhibit higher bromide solubility compared with their Mn^{2+} analogues, suggesting that the octahedral environment of Cd^{2+} can better accommodate lattice expansion induced by larger halides. In contrast, iodide incorporation remains limited because of its substantially larger ionic radius; for example, only ~6% I^- substitution has been reported in $Cs_4CdBi_2Cl_{12}$. Consistent with halide substitution trends in other perovskites, incorporation of less electronegative Br^- or I^- leads to a red shift in optical absorption and progressive band gap narrowing. For instance, the band gap decreases from 3.20 eV in $Cs_4CdBi_2Cl_{12}$ to approximately 2.99 eV in mixed-halide compositions such as $Cs_4CdBi_2Cl_{8.9}Br_{3.1}$, accompanied by a nearly linear increase in lattice volume due to the larger ionic radii of the substituted halides. Similar substitution limits of ~26% and ~29% bromide have been reported for $Cs_4CdBi_2Cl_{12}$ and $Cs_4CdSb_2Cl_{12}$, respectively.[56]

Halide substitution effects become particularly pronounced in nanocrystalline systems. For example, nanocrystals of $Cs_4CuSb_2Cl_{12-x}I_x$ synthesised using oleyl amine and oleic acid surfactants exhibit a monoclinic *C*2/*m* structure up to approximately 50% iodide incorporation. Beyond this threshold, structural instability emerges, leading to the coexistence of monoclinic and trigonal ($P\bar{3}m1$) phases. Importantly, the composition containing ~50% iodide shows enhanced optoelectronic performance, including higher responsivity and detectivity, which has been attributed to reduced trap state density and improved hole mobility. In contrast, phase-impure nanocrystals formed at higher iodide concentrations display inferior device performance.[34]

Consistent with these observations, increasing iodide content in $Cs_4CuSb_2Cl_{12}$ nanocrystals gradually narrows the band gap from ~1.96 eV to ~1.87 eV and induces a systematic red shift in both absorption and photoluminescence spectra. The lattice expansion associated with the substitution of Cl^- by the larger I^- anions further confirms the structural accommodation of heavier halides. While the parent chloride nanocrystals possess a monoclinic structure, the framework remains stable up to approximately 50% I^- substitution before secondary trigonal phases appear, highlighting a structural tolerance limit for iodide incorporation.[34]

In addition to heavier halides, incorporation of smaller anions such as F^- provides an alternative strategy for tuning structural and electronic properties.[101] Fluorine substitution has been reported to influence primarily the absorption characteristics and microstructural features of $Cs_4CuSb_2Cl_{12}$ thin films. Because of its small ionic radius and strong electronegativity, F^- reduces interlayer interactions and results in smaller crystallite sizes, as evidenced by peak broadening in X-ray diffraction patterns. Consequently, a slight blue shift in optical absorption is observed, accompanied by a modest increase in the band gap from 1.65 eV to ~1.70 eV. Beyond band gap modulation, fluorine incorporation also improves charge-transport properties by passivating defect sites that typically act as hole traps. F-doped films exhibit reduced hysteresis and enhanced carrier transport. Hall effect measurements further reveal increased carrier concentration, improved mobility, and enhanced electrical conductivity, indicating that halide substitution can simultaneously modulate both optical and electronic properties in LDPs.[40]

In addition to halide substitution, emerging strategies explore the incorporation of mixed anion frameworks, where halides coexist with chalcogenide anions. Mixed chalcogenide-halide perovskites have been proposed as promising lead-free alternatives in which chalcogenide (Ch = S, Se) and halide (X = Cl, Br, I) anions coexist within the same lattice. The stronger metal-chalcogenide bond compared to metal halide interactions is expected to enhance structural stability, particularly under humid conditions. Although incorporation of these materials remains limited and their synthesis often requires high temperatures, the split anion approach significantly expands the compositional space of LDPs.[27] Continued theoretical investigations together with experimental synthesis will be essential for understanding the structural chemistry and guiding the development of mixed chalcogenide-halide perovskites for future applications.

Overall, X-site engineering represents an effective strategy for tuning both the structural and optoelectronic properties of LDPs. While incorporation of larger halides such as Br^- and I-enables band gap narrowing and red-shifted optical absorption through lattice expansion and modified metal-halide orbital interactions, excessive substitution can induce structural instability or secondary phases. In contrast, incorporation of smaller ions such as F^- primarily influences defect passivation and charge transport, highlighting that X-site engineering provides a versatile pathway to simultaneously control the band structure, defect chemistry and material performance. Beyond halide substitution, developing mixed chalcogenide-halide systems further shows the possibility of stronger metal–chalcogen bonding to improve environmental stability while extending compositional flexibility. Collectively, these patterns suggest that the ionic size, electronegativity, and bonding type of X-site anions are essential parameters regulating the structural stability and optoelectronic performance of lead-free perovskites, offering useful guidance for future material design and optimization.

2.5 Compositional exploration through theoretical studies

Theoretical investigations play a crucial role in guiding the discovery and rational design of LDPs by predicting structural stability, electronic properties and feasible compositional spaces before experimental synthesis. Computational screening approaches commonly evaluate parameters such as Goldschmidt tolerance factor, octahedral factor, thermodynamic stability and electronic band structures to identify promising candidates for optoelectronic applications.

In a combined computational-experimental study, Vargas *et al.* explored potential LDP compositions for optoelectronic and photovoltaic applications by evaluating thermodynamic stability and electronic structures. Their screening identified nine potential LDPs, most exhibiting wide band gaps in the range of 2.7–3.6 eV, except for $Rb_4CuSb_2Cl_{12}$, which showed comparatively narrower band gap characteristics. Using solid-state synthesis and precipitation routes in acidic or polar solvents, five of the predicted compounds were successfully synthesised experimentally. However, attempts to synthesise chromium and iron-based analogues were unsuccessful, primarily due to the instability of the +2-oxidation state for these transition metals under typical synthesis conditions. The difference in precursor solubility and kinetic limitations during crystallisation may also contribute to the formation difficulties, highlighting the importance of coupling theoretical predictions with careful synthetic optimisation.[83]

Further theoretical insights were provided by Jian Xu *et al.* (2021), in which the hypothetical compound $Rb_4SnSb_2Br_{12}$ was investigated using first-principles calculations. Twelve distinct polymorphic forms were identified and classified according to local octahedral connectivity motifs. Significantly different electronic structures were exhibited by these polymorphs, resulting in band gaps spanning a wide portion of the visible spectrum. It was demonstrated in the study that the optoelectronic properties of layered perovskites can be effectively tuned by modifying structural parameters such as layer thickness and octahedral stacking arrangements. Such tunability renders these materials attractive candidates for van der Waals heterostructures and tandem solar cells, although the synthesis and fabrication of high-quality thin films remain a key experimental challenge.[102] Symmetry analysis combined with density functional theory (DFT) calculations was employed by Lin *et al.* to predict stable layered structures. $Cs_4CdSb_2Cl_{12}$ and $Cs_4CdBi_2Cl_{12}$ were identified as thermodynamically stable compounds and were subsequently synthesised using solvothermal methods. The calculated band gaps were in good agreement with experimental values, with 3.0 eV for $Cs_4CdSb_2Cl_{12}$ and 3.23 eV for $Cs_4CdBi_2Cl_{12}$. The slight increase in band gap upon replacing Sb^{3+} with Bi^{3+} reflects the influence of B-site cation electronic configurations on the conduction band structure, illustrating how theoretical calculations can guide the band gap tuning through compositional engineering.[48]

A systematic theoretical investigation on $Cs_4MSb_2X_{12}$-type perovskites (M = transition metal; X = Cl, Br, I) led to the identification of three thermodynamically stable candidates. Among them, $Cs_4CuSb_2Cl_{12}$ and $Cs_4MnSb_2Cl_{12}$ were successfully synthesised, while $Cs_4ScSb_2Cl_{12}$ remained a computational prediction. Notably, these materials exhibit antiferromagnetic ordering, making them suitable not only for photovoltaics but also for spintronic applications.[103] Earlier, Jian Xu *et al.* (2018) identified seven stable $Cs_4M(\text{II})B(\text{III})_2Cl_{12}$ LDPs ($Cs_4ZnSb_2Cl_{12}$, $Cs_4ZnBi_2Cl_{12}$, $Cs_4ZnBi_2Br_{12}$, $Cs_4CdSb_2Cl_{12}$, $Cs_4CdSb_2Br_{12}$, $Cs_4CdBi_2Cl_{12}$ and $Cs_4CdBi_2Br_{12}$) through first-principles calculations as promising p-type transparent conductors, owing to their light hole effective masses and intrinsic conductivity.[81] Recent computational studies have also explored mixed valence layered halide perovskites with the general composition $Cs_4M(IV)M(II)_2X_{12}$ (M = Ge or Sn; X = Cl or Br). Four Ge-based compounds were predicted to be both thermodynamically and dynamically stable: $Cs_4GeGe_2Cl_{12}$ ($C2/m$ and $R\bar{3}m$), $Cs_4GeGe_2Br_{12}$ ($R\bar{3}m$) and the mixed anion phase $Cs_4GeGe_2Cl_6Br_6$ ($R\bar{3}m$). In contrast, the corresponding Sn analogues were found to be dynamically unstable due to imaginary phonon modes associated with high-energy Sn 5s states. Halide substitution further influences dielectric and optical properties, where Br incorporation increases the static dielectric constant and improves optical absorption. Hybrid functional calculations revealed tunable band gaps ranging from 1.16 eV to 2.25 eV, with an unusual intermediate conduction band originating from Ge(IV) 4s orbitals.[104] These findings expand the compositional landscape of lead-free mixed valence layered perovskites and identify Ge–Br chemistry as particularly promising for optoelectronic applications.

These findings emphasise the need for continued efforts in synthesis and property–function correlation to realise their full potential across optoelectronic applications.[81] The formation energies of the materials will vary depending on the synthetic conditions, and it is found that some materials are stable in the nanoscale compared to their bulk counterpart.[90] Exploration of synthetic strategies through experiments and material compositions through computational studies is required for future development. A systematic assembly of elements capable of forming $A_4B(II)B(III)_2X_{12}$ is presented in Fig. 4.

3. Synthetic techniques

The synthetic strategy plays a critical role in determining the structural stability, morphology, and optoelectronic performance of LDPs (Fig. 5). Careful selection of synthetic routes enables control over crystal growth, defect formation, and dimensionality, thereby allowing the tuning of material properties for specific optoelectronic applications. In general, LDPs can be synthesised in a variety of morphologies, from bulk polycrystalline powders and single crystals to nanocrystals and thin films by employing suitable synthetic methods.

3.1 Bulk crystal synthesis

3.1.1 Precipitation method. The first member of the $A_4B(II)B(III)_2X_{12}$ family, $Cs_4CuSb_2Cl_{12}$, was first synthesised by Vargas *et al.* in 2017 using an acid precipitation method. The obtained material exhibited a broad absorption spectrum with a direct band gap of approximately 1 eV. In addition to its favourable optical properties, $Cs_4CuSb_2Cl_{12}$ demonstrated remarkable stability against light exposure, temperature variations, and moisture, together with simple solution processability, making it a promising candidate for optoelectronic applications.[25] Subsequent studies further optimised the precipitation approach by employing various polar solvents such as acetone, methanol, and ethanol to influence nucleation and crystal growth processes. These solvent environments can significantly affect crystallinity, particle morphology, and phase purity of the resulting materials.[28] Further modification of the synthesis protocol, involving the introduction of small amounts of water combined with ultrasonic treatment, led to products exhibiting an increased band gap of about 1.66 eV, indicating that synthesis conditions can strongly influence the electronic structure and optical behaviour of the material.[105] Using an appropriate solvent for washing is also important to get quality products. Some common solvents used for washing include acetone, ethanol, isopropanol, ethyl acetate, diethyl ether, *etc.*

3.1.2 Mechanochemical method. Mechanochemical synthesis has emerged as an alternative route for the preparation of

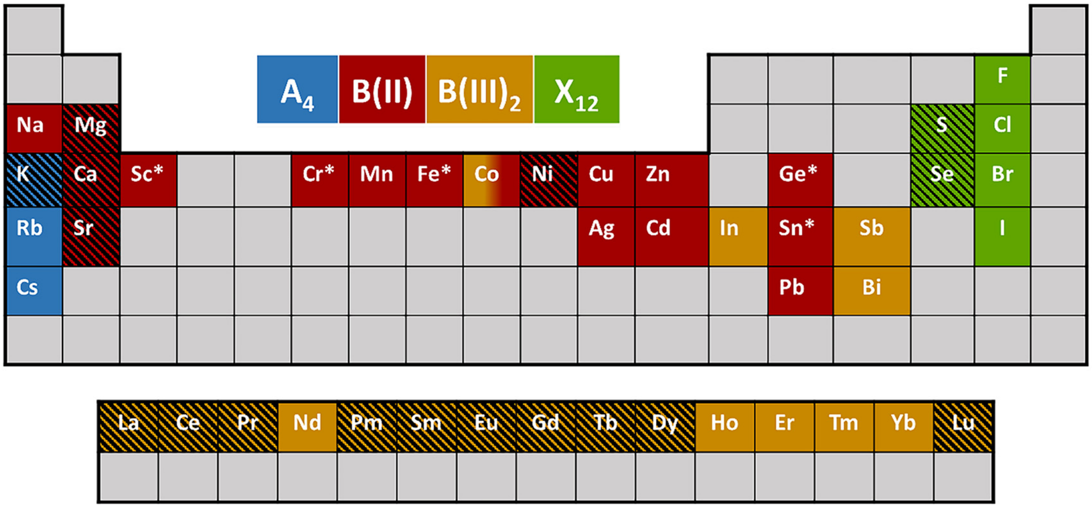

Fig. 4 Elements forming layered double perovskites with the composition $A_4B(II)B(III)_2X_{12}$. The colours specify the site occupied by the elements, according to the standard composition at the top. The elements marked with (*) denote the elements that have been computationally predicted to form stable products but need experimental validation. The elements marked with the lined pattern denote the elements that could be used in $A_4B(II)B(III)_2X_{12}$ composition but need to be explored through computational and experimental methods.

LDPs, offering a simple and environmentally friendly approach. In this method, the precursors are subjected to mechanical grinding, which promotes solid-state reactions through the application of mechanical energy. Notably, the synthesis can be carried out at room temperature without the need for solvents, making it a cost-effective and sustainable strategy for material preparation.

The LDP materials synthesised *via* mechanochemical grinding exhibit structural characteristics comparable to those obtained through conventional solution-processed methods. One of the key advantages of this technique is the high reaction efficiency, often yielding nearly quantitative conversion of precursors. Additionally, the resulting material demonstrates good thermal and chemical stability, remaining stable up to approximately 210 °C under ambient conditions.[28]

Despite these advantages, mechanochemical synthesis typically provides limited control over particle size distribution and morphology compared to solution-based nanocrystal synthesis methods. As a result, this approach is more suitable for the preparation of bulk or polycrystalline materials rather than highly uniform nanostructures required for certain optoelectronic applications.

3.1.3 Ball milling. A recent study by Zang *et al.* (2024) reported the synthesis of $Cs_4CuSb_2Cl_{12}$ through a precipitation method followed by ball milling as a post-synthetic size reduction strategy. By varying the milling duration from one to three hours, the particle size progressively decreased while the surface area increased. Notably, milling for three hours resulted in a nearly tenfold increase in surface area compared to the bulk crystals.[41]

Ball-milling the co-precipitated $Cs_4CuSb_2Cl_{12}$ crystals creates intense mechanical collisions that fracture the weak van der Waals-held layers, exposing the surface and ejecting chlorine atoms because the Cu–Cl bond has the lowest bond-energy in the lattice. The loss of Cl^- generates chlorine vacancies, and the vacancy-induced charge imbalance promotes partial reduction of nearby Cu^{2+} to Cu^+, as the missing Cl^- leaves excess electrons that localise on copper centres. These vacancy-related defect states introduce mid-gap energy levels, widening the absorption tail into the near-infrared and raising the electron concentration and mobility.[106]

Optical characterisation revealed a broad absorption feature with the absorption edge extending up to ~1100 nm. As the particle size decreased, the absorption intensity in the 900–1400 nm region increased significantly. Correspondingly, the band gap gradually decreased from 1.084 eV (bulk) to 1.066 eV and further to 1.026 eV after three hours of milling. This band gap narrowing and enhanced light absorption were directly associated with improved photocatalytic performance. Overall, the study demonstrates that ball milling serves as an effective top-down approach to tailor the optical properties by controlling particle size and surface area.[41]

3.2 Nanocrystal synthesis

Nanocrystals have attracted considerable interest due to their superior optical and electronic properties compared to bulk materials. The reduction in particle size introduces quantum confinement effects, enabling tunable band gaps and modified charge-carrier dynamics. As a result, nanocrystals often exhibit enhanced optical absorption, improved photoluminescence, and increased surface reactivity, making them favourable for applications in optoelectronics and photocatalysis. The structural and optoelectronic properties of nanocrystals strongly depend on parameters such as particle size, morphology and surface chemistry. Surfactants play a crucial role during synthesis by controlling nucleation and growth, stabilising surface atoms and providing colloidal stability, which in turn influences the photophysical properties of the nanocrystals.[107] Common synthetic approaches for LDP nanocrystals include the hot-injection method, ultrasonic exfoliation and solvothermal methods, each offering different levels of control over particle size, morphology and crystallinity.

3.2.1 Exfoliation method. The first report on the synthesis of $Cs_4CuSb_2Cl_{12}$ nanocrystals employed the exfoliation method. Xu-Dong Wang *et al.* (2019) for the first time synthesized $Cs_4CuSb_2Cl_{12}$ nanocrystals from bulk crystals through the ultrasonic exfoliation method. This top-down approach gives rise to the change from indirect to direct band gap when exfoliated from bulk to nano. As-synthesized nanocrystals with a narrow band gap of 1.6 eV and reduced electron effective mass are promising candidates for optoelectronic applications. Even though the exfoliation energy of both $Cs_3Sb_2X_9$ and $Cs_4CuSb_2Cl_{12}$ is similar, $Cs_4CuSb_2Cl_{12}$ nanocrystals show smaller, uniformly sized nanocrystals in comparison to $Cs_3Sb_2X_9$. This may be due to the weaker in-plane chemical bonds in $Cs_4CuSb_2Cl_{12}$, which makes the exfoliation process easier. They investigated the effect of solvents on ultrasonic exfoliation and found that the mixed solution of $CHCl_3$ and OA was the preferred solvent to acquire high-quality $Cs_4CuSb_2Cl_{12}$ NCs.[29]

The high-polarity solvents readily degraded the $Cs_4CuSb_2Cl_{12}$ nanocrystals, while low-polarity solvents showed better suspension quality. The size of the nanocrystals obtained varied from 3 nm to 25 nm in the non-polar or low polarity solvents. The higher concentration of $Cs_4CuSb_2Cl_{12}$ NC was observed in a non-chlorinated solvent, toluene, most likely due to its elevated boiling point. The darkest colour among the chlorinated solvents is observed in chloroform solution, which may be due to the generation of HCl through hydrolysis. The presence of HCl species may help weaken the interlayer forces, facilitating the separation of layers. The size of the $Cs_4CuSb_2Cl_{12}$ NCs was unaffected or scarcely varied with the centrifugation speed. The use of surfactants like oleic acid led to a notable transformation in the nanocrystals' morphology. The combined solution of chloroform and oleic acid was potentially suitable for obtaining high-quality nanocrystals.[29]

3.2.2 Hot injection method. The hot-injection method is one of the most widely employed techniques for the synthesis of nanocrystals, owing to its ability to provide precise control over particle size and morphology. Comparatively, this approach produces nanocrystals featuring superior size uniformity and dispersity over exfoliation methods. Oleic acid and oleyl amine

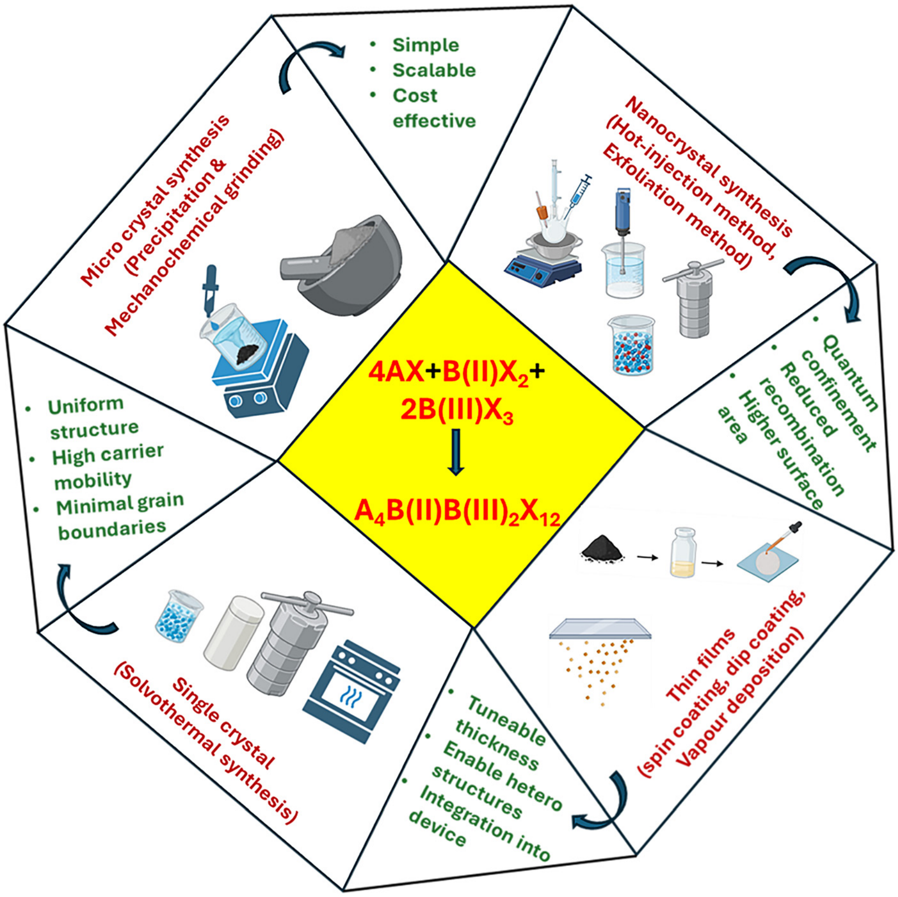

Fig. 5 Schematic representation of the influence of different synthetic methods on structure and optoelectronic properties of $A_4B(II)B(III)_2Cl_{12}$ LDPs.

surfactants guide morphology and enhance colloidal stability, facilitating precise control in perovskite nanocrystal synthesis.[32]

The first colloidal synthesis of lead-free layered double perovskite nanocrystals *via* the hot-injection method was reported by Ashitha *et al.* (2021) for $Cs_4CuSb_2Cl_{12}$. The synthesised nanocrystals crystallised in a vacancy-ordered monoclinic structure and exhibited a direct band gap of about 1.79 eV. The nanocrystals showed better crystallinity that facilitates efficient charge transport, along with good stability under ambient and thermal conditions, highlighting their potential for practical optoelectronic applications.[33]

To achieve better control over nanocrystal morphology, Mai *et al.* employed a modified hot-injection method for the synthesis of $Cs_4ZnSb_2Cl_{12}$ nanocrystals. By systematically adjusting parameters such as solvent composition, reaction temperature, precursor concentration, and reaction time, the morphology of nanocrystals could be tuned to obtain nanodots, nanowires, and nanoplatelets (Fig. 6(a)). In addition, surfactants such as oleic acid and oleyl amine played a crucial role as capping ligands by directing crystal growth and stabilizing the formed nanostructures. This ligand assisted growth enabled precise control over particle shape and size, which in turn influenced the optoelectronic properties of the material. The controlled nanostructures exhibited tunable optical absorption (Fig. 6(b) and (c)) and enhanced light–matter interaction compared to bulk materials, demonstrating the significant impact of nanoscale morphology on optoelectronic properties.[90]

Defect-related trap states, which dominate carrier loss in many perovskite nanomaterials, are markedly suppressed in these hot-injection-synthesized NCs. Unlike exfoliated $Cs_4CuSb_2Cl_{12}$ NCs that exhibit an ultrafast ∼14 ps defect-trapping component arising from incomplete surface termination,[29] the NCs synthesized through the hot injection method show no such fast trap and instead display longer lifetimes indicative of effective surface passivation.[108]

3.2.3 Effect of moisture.

The incorporation of water during synthesis enhances the photophysical properties, converting dark transitions into radiative ones. A moisture-assisted hot-injection method was developed by Liu *et al.* (2022) to synthesize these nanocrystals. This material exhibits a direct bandgap (3.56–3.82 eV), near-UV photoluminescence, and enhanced self-trapped exciton (STE) effects. Self-trapped excitons in $Cs_4CuIn_2Cl_{12}$ nanocrystals originate from a strong lattice distortion of the $[CuCl_6]^{4-}$ octahedra when an electron-hole pair is created. In the excited state the octahedron undergoes a Jahn–Teller type contraction of the four in-plane Cu–Cl bonds, which localises the exciton and lowers its energy relative to the free-exciton state, producing a large Stokes shift (∼108 nm) and a

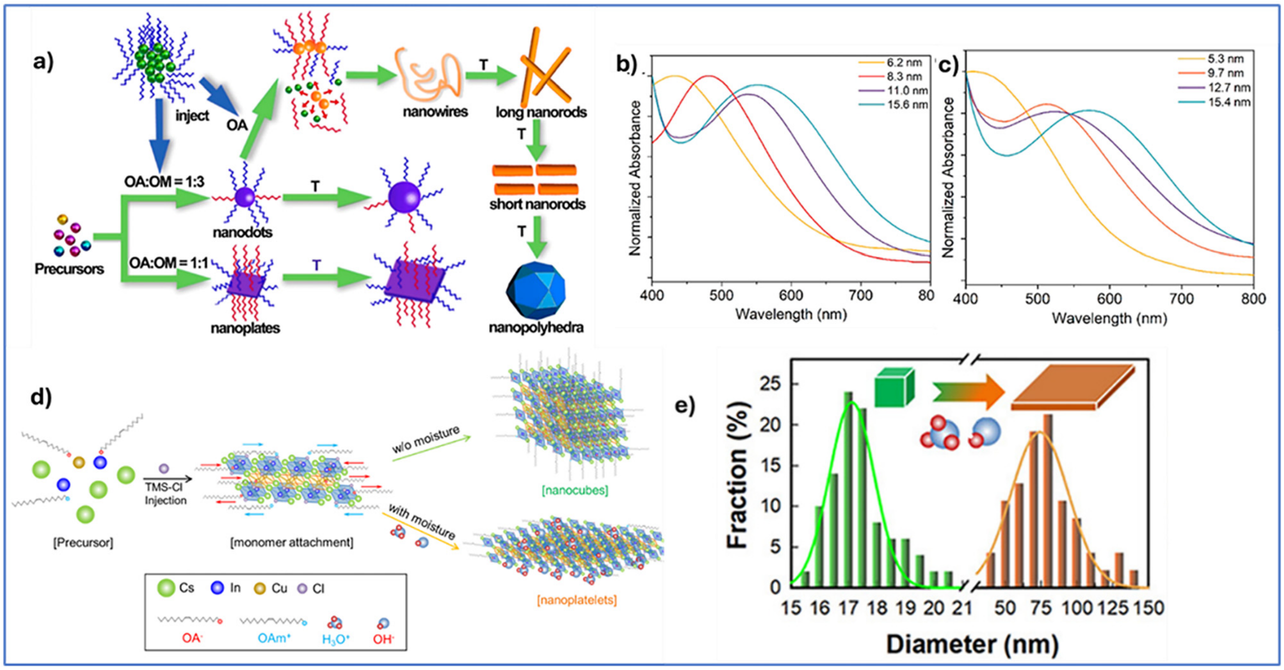

Fig. 6 Influence of synthetic parameters on the morphology nanocrystals. Schematic of the synthesis of $Cs_4ZnSb_2Cl_{12}$ nanocrystals with precise control over shape and size (a). Absorbance spectra of $Cs_4ZnSb_2Cl_{12}$ nanodots (b) and nanoplates (c) of varying particle size.[90] Effect of moisture on the synthesis of $Cs_4CuIn_2Cl_{12}$ nanocrystals (d). Size distribution plot of nano-cubes and moisture assisted nanoplates. (e)[75] Reprinted, with permission, from ref. 90 and 75.

broad, asymmetric emission band.[100] Moisture in the precursor (∼40% RH) supplies ionised H_3O^+ and OH^- that act as additional capping ligands, promoting the growth of 2D nanoplatelets rather than 3D nano-cubes (Fig. 6(d) and (e)). This morphological change enhances the excitonic contribution to absorption and strengthens the STE effect.[75]

3.2.4 Effect of the chloride source. To investigate the effect of the halide source on product formation, P. Ashitha *et al.* systematically introduced various chloride precursors into the reaction system. Initially, benzoyl chloride was used, which led to the successful formation of phase-pure $Cs_4CuSb_2Cl_{12}$ nanocrystals (NCs) without any modification to other reaction conditions. The chloride source was then substituted with benzyl chloride under the same conditions, and no product was formed, highlighting the importance of the chloride precursor in the success of NC synthesis. Finally, trimethylsilyl chloride (TMS-Cl) was employed as the Cl source, and in this case, the reaction proceeded successfully, yielding phase-pure $Cs_4CuSb_2Cl_{12}$ NCs once again.[33]

3.2.5 Effect of capping ligands. The effect of caping ligands and their concentrations on the formation and surface passivation of LDPs has been systematically investigated, particularly with respect to trap states and their influence on charge carrier dynamics. Capping ligands not only regulate crystal growth but also play a crucial role in passivating surface defects that act as trap states, thereby affecting the photophysical behaviour of the material. It was observed that a low concentration of oleyl amine is beneficial for both the synthesis and surface passivation, whereas a higher concentration inhibits crystal formation.[105]

Charge carriers can become trapped in localised electronic states within the band gap. These trap states are classified as shallow (near the band edge) or deep (closer to the middle of the band gap). Deep trap states are particularly detrimental as they can lead to non-radiative recombination and optical losses.[105] For instance, ultrafast charge-carrier trapping processes, occurring in as little as 1.4ps, have been identified as a limitation in quadruple-perovskite nanocrystals.[55] Surface defects in $Cs_4CuSb_2Cl_{12}$ microcrystals also contribute to carrier trapping, limiting optoelectronic performance. The relaxation of photogenerated carriers is a complex process influenced by factors like alloying and surface passivation.[105]

In comparative studies, $Cs_4CuSb_2Cl_{12}$ microcrystals were synthesised using different capping ligands, including oleic acid (OA), oleyl amine (OAm), and trioctylphosphine (TOP), by varying their concentrations. OA was found to support the product formation even at relatively higher concentrations (1–12%), indicating its compatibility with the crystal growth process. In contrast, the use of TOP did not yield the characteristic black precipitate, suggesting unsuccessful crystallisation. Similarly, increasing the concentration of OAm from 1–2% prevented the precipitate formation, implying that excessive OAm suppresses nucleation and growth of $Cs_4CuSb_2Cl_{12}$ crystals. This behaviour is attributed to the relatively larger molecular size of OAm, which can introduce steric hindrance between precursor species, thereby restricting effective crystal formation.[106]

The comparative investigation of several nanocrystal synthesis procedures demonstrates that the synthetic process greatly influences the shape, crystallinity, defect density and hence the optoelectronic performance of LDPs. Top-down methods such as ultrasonic exfoliation are useful for creating nanostructures with reduced effective mass and configurable band gaps. Whereas bottom-up methods such as hot-injection synthesis allow superior control over particle size, shape and surface passivation. Among the reported approaches, colloidal hot-injection synthesis generally delivers extremely uniform and crystalline nanostructures with better optical absorbance and optoelectronic performance due to fine control over nucleation and growth kinetics. Across these studies, some common design principles can be identified for the synthesis of LDP nanocrystals. Control over dimensionality and particle size is critical for tailoring the band structure and charge carrier dynamics, while the ligand engineering plays a vital role in regulating crystal formation and minimising surface trap states. In addition, solvent polarity and precursor chemistry substantially influence nanocrystal stability, morphology, and phase formation. Improved crystallinity along with good defect passivation is crucial for achieving enhanced photophysical and photocatalytic performance. Overall, these observations suggest that rational control of synthesis parameters is crucial for forming high-performance LDP nanocrystals for optoelectronic and energy related applications.

3.3 Water-oil biphasic method

A novel water-oil biphasic method for synthesising lead-free double perovskite nanocrystals was developed by Liu *et al.* In this approach, the transformation from 0D Cs_3BiBr_6 to 2D $Cs_4ZnBi_2Br_{12}$ was achieved in a two-step process. Initially, Cs_3BiBr_6 nanocrystals (NCs) were synthesised using the conventional hot-injection method. Then, a controlled volume of $ZnBr_2$ aqueous solution (1.5 μL of 4 g mL^{-1}) was added to 2 mL of the Cs_3BiBr_6 NC dispersion. The resulting biphasic mixture was stirred at 400 rpm for 30 minutes at room temperature. After allowing phase separation for one minute, the upper toluene layer was collected and centrifuged at 4000 rpm for 5 minutes.[74]

This biphasic system offers a controlled reaction environment that enhances nanocrystal formation by minimising structural damage and facilitating impurity removal. The immiscible phases serve unique functions; the aqueous phase allows for fine control of ionic concentrations and cation delivery, whereas the toluene phase stabilises the developing nanocrystals. Interfacial ligands act as molecular bridges, facilitating ion transfer across phases and encouraging uniform nucleation.[109,110]

By restricting the reaction to the interface, this approach produces nanocrystals with higher crystallinity, structural stability, and lower impurity levels than conventional single-phase synthesis. The aqueous phase also serves as a sink for byproducts, aiding in the purifying procedure. Furthermore, the controlled growth kinetics and stabilising ligand environment contribute to the long-term environmental stability of the NCs. This method enables real-time monitoring of nanocrystal transformations and offers valuable insights into cation exchange processes and structural evolution.[111,112]

3.4 Hydrothermal method

Single crystals (SCs) of layered double perovskites can be grown under controlled temperature and pressure using hydrothermal methods. Polycrystalline $Cs_4CuSb_2Cl_{12}$ is first synthesised through a solid-state reaction by heating stoichiometric amounts of CsCl, $CuCl_2$, and $SbCl_3$ at 220 °C for 3days. The resulting polycrystalline material serves as a precursor for single-crystal growth. For the hydrothermal process, the precursor is mixed with hydrochloric acid, sealed in a Teflon-lined stainless-steel autoclave, heated gradually to 150 °C, maintained for 3 days, and then slowly cooled to room temperature. This procedure produces dark purple triangular single crystals suitable for structural and optical characterisation.[54,113]

Similarly, $Cs_4MnBi_2Cl_{12}$ single crystals were synthesised, and they exhibited orange photoluminescence under illumination with a photoluminescence quantum yield of about 25.7% at 610 nm, originating from the d–d transition of Mn^{2+} emissive centres. In contrast, microcrystals of the same compound prepared *via* an acid-precipitation method with layered wafer morphology show a lower PLQY of 7.8%. The enhanced PLQY in single crystals is attributed to improved crystallinity, reduced trap state density, and fewer grain boundaries.[91,114]

The solvothermal approach has also been extended to the synthesis of nanocrystals, typically employing organic capping ligands to control nucleation and particle growth.[35]

3.4.1 Effect of pressure. Yalin Ma *et al.* provided a unique strategy to tune the band gap of the lead-free layered double perovskites by the application of pressure. Under normal conditions, the transparent and colourless $Cs_4MnBi_2Cl_{12}$ LDP single crystals had a direct band gap of 3.26 eV. The band gap rapidly dropped with increasing applied pressure, reaching 2.87 eV at 13.5 GPa and 2.10 eV at 15.6 GPa. As a result, the crystal's colour shifted from translucent light orange to red. When the pressure was increased further, a dramatic band gap widening to 2.25 eV occurred at 17.5 GPa, followed by another round of band gap narrowing from 2.25 to 2 eV when the pressure reached its peak of 33.9 GPa.[54]

3.5 Film preparation

3.5.1 Solution-based method. Solution-processed thin films are generally prepared using polar aprotic solvents, which can dissolve ionic metal-halide precursors. Zang *et al.* reported the preparation of $Cs_4CuSb_2Cl_{12}$ thin films using dimethyl sulfoxide (DMSO) as the primary solvent, followed by spin-coating deposition and annealing. DMSO is widely preferred due to its relatively low toxicity, high boiling point, and strong coordinating ability, which slows crystallisation and promotes uniform film formation.[115,116]

Another commonly used solvent is dimethylformamide (DMF), although it is more volatile and toxic than DMSO. The solubility of metal halide precursors is less in DMF in comparison to DMSO due to its strong ionic lattice. Consequently, mixed solvent systems such as DMF/DMSO are frequently employed to balance solubility and crystallisation kinetics. Such solvent combinations have also been successfully used for depositing related layered and double perovskite films, including $Cs_3Sb_2I_9$ and $Cs_2AgBiBr_6$.[117] Careful control of thermal annealing is required to ensure slow crystallisation and obtain uniform films. In contrast, polar protic solvents such as water, methanol, ethanol and isopropanol are generally unsuitable as primary solvents for film preparation. Their high volatility and low boiling points tend to induce rapid precipitation rather than controlled film growth, often resulting in rough or discontinuous films.[118]

Similarly, non-polar solvents such as toluene, hexane, and chlorobenzene cannot dissolve LDP precursors because of the compound's ionic and polar nature. Films prepared directly from such dispersions are typically uneven or cracked. However, these solvents play an important role as antisolvents during spin coating, where they assist in the rapid removal of the primary solvent and promote controlled crystallisation.[119,120] Among them, toluene and chlorobenzene are the most appropriate antisolvents used for the synthesis of pin-hole free, smooth and uniform films, and they enable good removal of the primary solvents.[121,122]

Despite these strategies, the fabrication of LDP thin films remains challenging due to poor precursor solubility, rapid crystallisation, and precipitation during processing. As a result, vapour-phase deposition methods such as aerosol-assisted chemical vapour deposition (AACVD) are often considered more reliable for obtaining uniform films, owing to their scalability, simplicity and better control over film growth.[40]

3.5.2 Aerosol-assisted chemical vapour deposition (AACVD) method. The *in situ* preparation of films by the AACVD method is applied for the first time by Balderas *et al.* The AACVD technique employing a double-source system was utilised to deposit both pristine and F-doped $Cs_4CuSb_2Cl_{12}$ films. This dual-source approach is essential because certain precursors, such as CsCl, can react and precipitate when mixed in a single solution, which hinders uniform film formation. By keeping the precursors in two separate solutions, the technique enables their simultaneous nebulization and delivery to the substrate without premature reaction.[74,123]

Each precursor solution is nebulised into fine droplets before being sent to a nozzle chamber *via* a nitrogen gas stream. A secondary nitrogen flux is used to dilute the aerosol and send it to a heated substrate, where solvent evaporation causes film nucleation and growth. The method facilitates *in situ* formation of continuous perovskite films, effectively addressing challenges like low solubility and rapid crystallisation that limit solution-based methods such as spin coating.[124,125]

AACVD stands out for its simplicity, scalability, and cost-effectiveness, as well as its versatility in doping, which can be achieved by simply introducing dopant salts into the precursor solutions. The choice of solvent system is critical for phase purity; a mixture of propan-2-one and propan-2-ol was found to yield phase-pure films for both undoped and F-doped compositions. This AACVD-deposited perovskite material was subsequently employed in photoconductive devices, with films deposited onto substrates patterned with interdigitated gold electrodes.[126]

3.5.3 Suspension quality. The suspension stability of LDPs has also been evaluated in different solvents. High-polarity solvents were found to induce degradation, for example, when suspended in isopropanol the materials got degraded and turned yellow. The suspension with chloroform was also not good as the product was settled down within 30–60 min.[127] The better suspension quality was observed in low polarity chlorobenzene and non-polar toluene.[106] The interaction between solvents and precursors can be rationalized using Gutmann's donor number (DN), which quantifies the Lewis basicity of a solvent and its coordination strength toward metal precursors. Solvents such as dimethyl sulfoxide (DMSO), *N*-methyl-2-pyrrolidone (NMP) and dimethylformamide (DMF) possess high DN values due to their strong Lewis basicity. These solvents are good in producing stable precursor solutions, which is useful for thin film deposition. On the other hand, solvents with low DN values such as propylene carbonate (PC), acetonitrile (ACN), and tetramethyl sulfone (TMS) promote crystallization and are hence appropriate for single crystal growth.[27]

3.5.4 Challenges in thin film formation and scalability. For the preparation of LDP thin films, a number of deposition techniques have been investigated, including spin coating, vapour deposition, and aerosol-assisted chemical vapour deposition; nonetheless, obtaining high-quality films appropriate for large-area device fabrication continues to be a significant issue. Thin-film engineering is an essential component of material development since film shape, crystallinity, and defect density have a significant impact on the performance of LDP-based optoelectronic devices.

One of the primary challenges is film uniformity and phase purity. Nonuniform nucleation and uncontrolled crystallisation are common problems in solution-processed perovskite films, leading to uneven film shape and insufficient substrate coverage. Rapid solvent evaporation during spin coating can create nanoscale inhomogeneities and defective clusters that degrade optoelectronic properties and device performance. Post-annealing or vapor-assisted treatments have been shown to promote grain growth and reduce these structural irregularities in perovskite films.[128] Another critical issue is defect formation within the bulk and at interfaces. Polycrystalline perovskite films typically contain vacancies, antisite defects, and interstitials that act as trap states for charge carriers. These defects significantly influence the recombination process and reduce material performance.[129] Simulation studies on $Cs_4CuSb_2Cl_{12}$-based photovoltaic devices indicate that increasing bulk defect density dramatically decreases open circuit voltage, current density, and power conversion efficiency due to enhanced carrier recombination.[130] Therefore, controlling defect density through precursor chemistry, optimised annealing conditions, and compositional engineering is essential for improving material performance.

Closely related to defect formation is the presence of grain boundaries in polycrystalline films. Grain boundaries often act as recombination centres because they contain a high density of structural defects and dangling bonds. These regions can trap charge carriers and hinder their transport across the film, thereby reducing charge collection efficiency. In addition, grain boundaries can serve as pathways for environmental degradation under moisture, heat or illumination. Strategies such as compositional engineering, additive incorporation and surface passivation have been widely investigated to mitigate grain boundary defects and enhance film stability.[131] Increasing grain size through controlled crystallisation is also an effective approach, as larger grains generally correspond to lower trap density and improved carrier transport.

Controlling crystallisation kinetics is crucial for LDP thin films because many layered perovskites possess strong ionic bonds and low precursor solubility. These traits often cause rapid nucleation and uncontrolled precipitation during solution processing, resulting in films with incomplete surface coverage and irregular grain shapes. To overcome this, approaches such as solvent engineering, antisolvent treatment, and vapor-assisted crystallization have been employed to modulate nucleation and achieve uniform crystal growth.[129]

From a practical perspective, scalability and compatibility with large-area processing techniques represent another major bottleneck. While many studies on perovskite thin films have been performed in a laboratory setting *via* spin coating or drop casting, these methods are inherently confined to small areas and not compatible with industrial-scale processing. On the other hand, large area coating processing techniques such as blade coating, slot-die coating, spray coating and chemical vapour deposition are compatible with fabrication of perovskite films on large areas. However, maintaining film uniformity and controlled crystallisation over large substrates remains challenging because slight variations in solvent evaporation, temperature gradients or precursor concentration can lead to thickness fluctuations and defect formation.[132]

Furthermore, interface quality between the perovskite layer and charge transport layers plays a decisive role in device operation. High densities of interface defects can introduce trap states that increase recombination and reduce device efficiency. Studies have shown that even a moderate increase in interface defect density can significantly degrade photovoltaic performance, highlighting the importance of interfacial engineering and surface passivation strategies for device optimisation.[130] Overall, the development of scalable LDP thin films requires a combination of controlled crystallisation, defect passivation and large area deposition techniques. Future research should focus on understanding the structure-processing-property relationships governing the thin film formation in LDPs, enabling the design of deposition methods that simultaneously ensure uniform morphology, low defect density, and compatibility with large scale manufacturing processes.

4. Applications for LDPs

The large compositional space and strong structural tunability of LDPs give rise to a wide range of optoelectronic properties. Moreover, when compared to traditional lead-based perovskites, heterometallic halide LDPs show better environmental stability, which makes them attractive options for a variety of functional applications. As a result, their potential in a variety of optoelectronic and energy-related technologies has been the subject of numerous investigations in recent years. Recent developments in the application of LDPs in light-emitting diodes (LEDs), photodetectors, photovoltaics, photocatalytic CO_2 reduction, and photothermal energy conversion are outlined in the following sections.

4.1 Light emitting diodes (LEDs)

LDPs have been investigated as potential phosphors for white LED applications because of their better environmental stability, easy production, and good emissive qualities. For instance, $Cs_4MnBi_2Cl_{12}$ single crystals exhibit efficient Mn^{2+} based orange red emission with good PLQY and high resistance to heat, moisture and continuous illumination, enabling their use as red phosphor in phosphor converted white LEDs (Fig. 7(a)).[51] Emission performance can be significantly improved through compositional engineering. For example, In^{3+} substitution at the Bi^{3+} site in $Cs_4MnBi_2Cl_{12}$ induces lattice distortion of the $[MnCl_6]^{4-}$ octahedra, strengthening the local crystal field around Mn^{2+} and producing a red shift of the Mn^{2+} emission band from 606 nm to 616 nm.[53] Phosphor converted LEDs fabricated using $Cs_4MnBi_2Cl_{12}$ and $Cs_4Mn(Bi_{0.88}In_{0.12})_2Cl_{12}$ show improved device performance, with colour rendering indices (CRI) of 82–86 and correlated colour temperatures around 4280–4510 K, along with an expanded colour gamut.[53] Similarly, Ag^+ doping in $Cs_4CdBi_2Cl_{12}$ markedly enhances broad band orange emission by suppressing exciton–phonon coupling and non-radiative recombination associated with self-trapped excitons, enabling white LEDs with CIE coordinates of (0.31, 0.34), a high CRI of $\sim$90, and stable operation for extended periods.[67] In addition, rare earth ion (RE^{3+} = Nd, Ho, Er, Tm) incorporation in Mn-containing layered perovskites such as $Cs_4Mn_{1-w}Cd_wBi_2Cl_{12}$ introduces characteristic red and NIR emissions.[60] Such systems enable full-spectral emission spanning the visible and NIR regions and yield phosphor-converted LEDs with significantly enhanced CRI values (up to $\sim$93).[64] These studies collectively demonstrate that heterovalent doping and rare-earth sensitisation provide effective routes to tailor emission colour, improve quantum efficiency, and expand the spectral coverage of LDP, highlighting their growing potential as stable phosphor materials for optoelectronic devices.

4.2 Photodetectors

LDPs have also demonstrated promising performance in photodetection applications due to their favourable carrier transport and defect tolerant electronic structures. For example, $Cs_4CdSb_2Cl_{12}$ NCs exhibit ultrafast carrier dynamics, enabling highspeed photodetectors with a photocurrent rise time of $\sim$25 ps and carrier lifetime of $\sim$150 ps. The photocurrent intensity is more than three orders of magnitude higher than the dark current, indicating efficient photo-carrier generation and transport.[32] Similarly, the $Cs_4CuSb_2Cl_{12}$ NC thin film photodetector

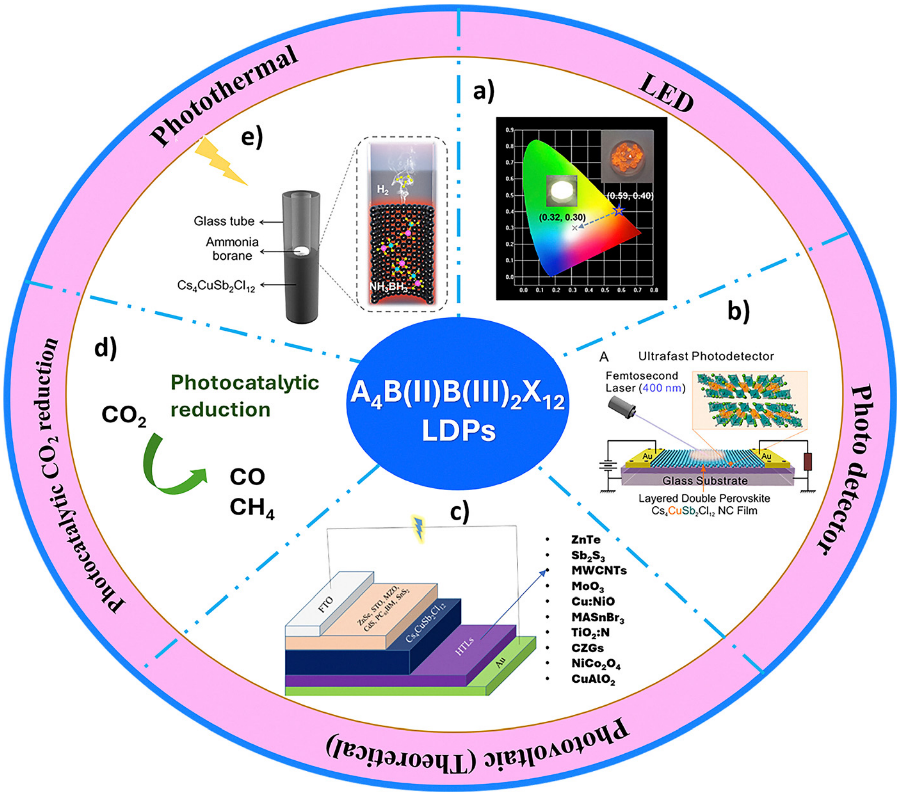

Fig. 7 Applications of LDPs. Representation of $Cs_4MnBi_2Cl_{12}$ for LED applications (a).[91] Depiction of $Cs_4CuSb_2Cl_{12}$ nanocrystals in high-speed photodetector devices (b).[89] Theoretically predicted device structure for $Cs_4CuSb_2Cl_{12}$ with different charge transport layers (c).[133] A schematic of photocatalytic CO_2 reduction (d). Illustration of photothermal energy conversion (e).[134] Reprinted with permission from ref. 91, 133, 134, and 30.

(Fig. 7(b)) shows ultrafast response with lifetimes around 150 ps and bandwidths approaching 10 GHz, attributed to efficient charge transport within the layered structure.[89] In contrast, microcrystalline $Cs_4CuSb_2Cl_{12}$ devices typically exhibit slower photo-response (rise and fall times in the millisecond range) but maintain good sensitivity, with detectivity values of the order of 10^8 Jones and responsivity of 10^{-3} A W^{-1}.[31] Partial halide substitution also enables photodetection functionality where the resulting device of $Cs_4CuSb_2Cl_6I_6$ exhibits a responsivity of 0.67 A W^{-1} and detectivity of 4.55×10^8 Jones.[34] Compositional engineering further enhances device performance; for instance, alloyed $Cs_4Mn_{0.25}Cd_{0.75}Bi_2Cl_{12}$ NCs exhibit significantly improved responsivity ($\sim 0.98 \times 10^8$ A W^{-1}) and quantum efficiency of 3×10^6% due to enhanced crystallinity, reduced trap density and longer carrier lifetimes.[55] These studies collectively demonstrate that structural tuning and nano-structuring in LDPs can effectively optimize charge transport and carrier dynamics, enabling their use in high-speed and highly sensitive photodetectors.

4.3 Photovoltaics (theoretical studies)

The photovoltaic potential of LDPs having a narrow bandgap suitable for solar absorbing materials such as $Cs_4CuSb_2Cl_{12}$ has been extensively explored through theoretical investigations. Device optimization studies using the Solar Cell Capacitance Simulator (SCAPS-1D) software have evaluated the influence of different charge transport layers and device parameters on solar cell performance. Simulated device architectures employing $CuSbS_2$/NiO and CNTS/NiO as hole transport layers demonstrated efficiencies of 19.88% and 19.95%, respectively (Fig. 7(c)).[133] Moreover, theoretical efficiencies approaching 30% were achieved through the use of CuSCN as the hole transport layer and SnO_2 as the electron transport layer. SCAPS-1D software was used to investigate 224 device designs with different parameters such as layer thickness, defect density, and doping concentration.[135]

Despite promising features, $Cs_4CuSb_2Cl_{12}$-based simulated solar cells have low carrier separation efficiency, which restricts total performance. To address this, a gradient doping approach was developed and optimized using SCAPS simulations. Tuning absorber thickness and doping concentration resulted in a power conversion efficiency of 24.4% at 400 K.[136] Furthermore, Pritam *et al.* simulated a tandem solar cell configuration comprising two top cells made of $Cs_4CuSb_2Cl_{12}$ and $Cs_2AgBiBr_6$ as absorber materials, and a bottom cell of crystalline silicon. The results underscore the potential of lead-free layered double perovskites as viable additives in high-efficiency solar devices.[43]

It is important to note that the above results are based on computational studies and have not yet been fully validated through practical device fabrication. In addition to simulation studies, a recent experimental study by Hoseinpour *et al.* has demonstrated the potential of these materials in solar cells.

$Cs_4CuSb_2Cl_{12}$ microcrystals, with a suitable band gap of ∼1 eV and broad absorption range, have been utilized as additives in lead-based solar cell devices. Incorporation of just 1% $Cs_4CuSb_2Cl_{12}$ into the active layer significantly enhanced both the efficiency and long-term stability of the device.[38]

In parallel, $Cs_4ZnSb_2Cl_{12}$ perovskites have demonstrated improved optoelectronic capabilities due to the insertion of Zn^{2+}, which introduces vacant Zn 4s orbitals into the conduction band minimum. This results in a decreased electron effective mass compared to counterparts like $Cs_4CuSb_2Cl_{12}$, where the conduction band is created by more localized Cu 3d orbitals. The lower carrier effective mass in $Cs_4ZnSb_2Cl_{12}$ facilitates improved charge transport and shows better toluene to benzaldehyde conversion further supporting its potential for photovoltaic applications.[90]

Although these forecasts are promising, experimental realization is still limited by difficulties in producing high-quality thin films and achieving efficient carrier separation. Defect-induced recombination and suboptimal charge transport also need to be resolved to unlock their full photovoltaic potential. Ongoing advances in compositional engineering and thin-film fabrication are expected to enhance practical performance. With further material and device optimization, $A_4B(\text{II})B(\text{III})_2X_{12}$ LDPs could become attractive, environmentally friendly candidates for next-generation photovoltaic technologies.

4.4 Photocatalytic CO_2 reduction

Photocatalytic CO_2 reduction efficiency in lead-free halide LDPs has been greatly boosted using several techniques such as nano-structuring, cation replacement, and alloying. For instance, $Cs_4CuSb_2Cl_{12}$ nanocrystals synthesized *via* coprecipitation followed by ball milling exhibit improved activity (72.17 $\mu mol\ g^{-1}$) compared to the bulk material (45.01 $\mu mol\ g^{-1}$). This enhancement is attributed to reduced particle size, increased surface area, high defect density, and broad-spectrum absorption, all of which contribute to a greater number of active catalytic sites.[137]

In $Cs_4MnSb_2Cl_{12}$, the incorporation of copper drastically alters the photocatalytic behaviour. Even small amounts of Cu^{2+} insertion led to significant improvements in CO_2 reduction. The best composition, $Cs_4Mn_{0.7}Cu_{0.3}Sb_2Cl_{12}$, achieves high CH_4 and CO yields of 68.35 and 503.86 $\mu mol\ g^{-1}$ respectively. However, additional increases in Cu^{2+} content result in lower product yields, highlighting the significance of precise dopant tuning for peak performance.[68] Adding Cu^{2+} in $Cs_4Cd_{0.8}Cu_{0.2}Bi_2Cl_{12}$ also improves photocatalytic CO_2 reduction, resulting in a CH_4 yield of 8.78 $\mu mol\ g^{-1}$ and a high selectivity of 95.78%. This is ascribed to Cu^{2+}-induced increase in charge separation, higher density of surface-active sites, and stabilization of critical reaction intermediates such as *COOH and *CO, which effectively direct the reaction route toward CH_4 generation under visible light.[72]

Similarly, Sb^{3+} insertion in $Cs_4MnBi_2Cl_{12}$ increases photocatalytic activity by improving light absorption, lowering spin–orbit coupling and Jahn–Teller effects and stimulating electronic delocalization. This reduces undesired electron transport to Mn^{2+} centres, resulting in lower fluorescence but greater charge carrier separation. The material attains a CO_2 reduction rate of 35.1 $\mu mol\ g^{-1}\ h^{-1}$ with 100% selectivity and allows simultaneous water oxidation to form H_2O_2, revealing the multifunctional catalytic potential of mixed cation systems.[66] $Cs_4CdBi_2Cl_{12}$ further illustrates the impact of composition on performance, surpassing its Sb counterpart ($Cs_4CdSb_2Cl_{12}$) due to higher surface area, improved CO_2 adsorption, greater reduction potential, and more efficient charge separation. This results in higher CO and CH_4 yields and a CO selectivity of 97.2%, compared to 89.9% in the Sb analogue.[71]

Recently, cobalt doped perovskites like $Cs_4MnCo_{0.9}Bi_{0.1}Cl_{12}$ demonstrated outstanding photocatalytic behaviour, achieving a CO yield of 69.16 $\mu mol\ g^{-1}\ h^{-1}$, which is 177 times higher than that of the undoped counterpart. This substantial improvement originates from cobalt induced spin polarization, which provides an internal electric field that enables charge carrier separation, suppresses recombination, and prolongs carrier lifetime-critical factors for achieving high photocatalytic efficiency.[70]

In photocatalytic CO_2 reduction, gas–solid systems are generally preferred over liquid–solid systems due to their improved catalyst stability. However, this configuration limits the formation of valuable liquid-phase products such as formic acid, methanol, formaldehyde and ethanol, which possess higher energy densities and greater potential for downstream applications. Addressing this limitation requires the development of more water stable LDP compositions and the design of photocatalytic systems capable of operating efficiently in mild and environmentally benign reaction media.[138]

Encapsulation strategies have emerged as effective approaches to address the stability limitations of lead-free perovskites while also improving charge carrier dynamics. Several studies have demonstrated the incorporation of these materials into protective matrices such as zeolites,[139] metal organic frameworks (MOFs),[140] or mesoporous oxides[141] to shield them from moisture and light-induced degradation. Furthermore, a detailed study of the strategies for the enhancement of photocatalytic solar fuel production was performed by Xie *et al.* in their recent review.[142]

4.5 Photothermal production of hydrogen

Wang *et al.* (2024) demonstrated the first example of utilizing layered double perovskite $Cs_4CuSb_2Cl_{12}$ microcrystals as the photothermal material with narrow band gap and lower thermal conductivity for the rapid hydrogen production (Fig. 7(e)).[29] The material is capable of absorbing full spectrum solar radiation and exhibits solar-thermal efficiency up to 93.4%. The rapid hydrogen production from ammonia borane was achieved by the high photothermal performance of the material that provides a new application for halide perovskites as photothermal converters.[134] This work opens up a new field of novel research for the metal halide layered double perovskites.

4.6 Photo-thermoelectric energy harvesting

The integration of $Cs_4CuSb_2Cl_{12}$ with MoS_2 enhances photothermal (PT) energy conversion through a synergistic interaction. $Cs_4CuSb_2Cl_{12}$ provides strong light absorption, especially in the near-infrared (NIR) region, and exhibits low thermal conductivity (<0.32 W m^{-1} K^{-1}), promoting localized heating. In contrast, MoS_2 has high thermal conductivity (155 W m^{-1} K^{-1}), aiding efficient heat dissipation. The composite benefits from the properties of both materials, including better optical absorption, thermal transport, and film compactness. A 75% $Cs_4CuSb_2Cl_{12}$ composition achieves optimal photothermal performance by balancing heat localization and thermal conduction, resulting in a better temperature difference (ΔT) and increased photothermal conversion efficiency. The composite films preserved phase purity and higher MoS_2 content improved packing density, further improving photothermal properties.[46] These results highlight the potential of LDP-based composites for efficient photothermal energy conversion and broaden their scope toward advanced energy harvesting applications.

5. Challenges and future perspectives

Despite the rising curiosity in lead-free LDPs with the general formula $A_4M(\text{II})M(\text{III})_2Cl_{12}$, various difficulties remain to limit its broad application and full potential in optoelectronic and energy conversion technologies. Addressing these issues requires a systematic roadmap that distinguishes short-term achievable goals from long-term fundamental research directions.

5.1 Short-term research priorities

(i) Expanding compositional diversity: the compositional landscape of LDPs remains largely unexplored, as most reported systems are restricted to Cs^+ at the A-site and Cl^- at the X-site. Expanding the compositional diversity through A-site substitution with other alkali cations (*e.g.*, Rb^+, K^+) and X-site engineering using Br^-, I^-, or split anion approach could enable improved bandgap tunability, structural flexibility, and environmental stability. In addition, B(II)-site engineering through incorporation of other transition-metals (Ni^{2+}, Zn^{2+}, Fe^{2+}, Co^{2+}...) and lanthanide substitution at the B(III) positions may further tailor luminescence, band structure alignment, and carrier dynamics. Such compositional modifications represent accessible strategies that can rapidly broaden the library of functional LDP materials.

(ii) Improving environmental stability: operational instability in humid environments and polar solvents remains a major drawback of LDPs. Exposure to moisture can cause structural degradation, and instability in polar media hampers electrochemical studies. Near-term approaches such as encapsulation, surface passivation, and incorporating hydrophobic binders or protective matrices during material preparation can markedly improve environmental stability and enable reliable material performance.

(iii) Thin film fabrication and property investigation: the optoelectronic properties of LDPs have been predominantly investigated in powder or bulk crystalline forms. However, these properties can differ significantly in thin-film configurations, which are more relevant for device applications. Therefore, systematic studies on the growth and characterization of high-quality LDP thin films are necessary. Additionally, investigations into defect states and their passivation remain limited, and deeper understanding in this area could significantly improve the performance of LDP-based optoelectronic devices. Future research should prioritize systematic investigations of defect states and their passivation, along with detailed exploration of the optoelectronic properties of LDPs in thin-film configurations relevant to device applications.

(iv) Development of scalable synthetic strategies: achieving precise stoichiometry and compositional homogeneity, particularly for nanocrystals and thin films, remains challenging. Many reported synthesis routes also suffer from limited reproducibility and scalability. Optimizing synthetic protocols and developing scalable deposition techniques for thin films will therefore be essential for translating LDP materials from laboratory studies to practical applications.

5.2 Long-term fundamental challenges

(i) Discovery of new material systems: exploring mixed-anion or chalcogenide-based layered perovskites such as partially substituting halides with S^{2-} or Se^{2-} could greatly broaden the structural and electronic landscape of LDPs. Likewise, introducing larger organic cations like MA^+ or FA^+ at the A-site may generate new structural motifs and alter electronic properties. A combination of computational screening and experimental validation will be essential for discovering these next-generation materials.

(ii) Heterostructure design: hybrid heterojunctions that integrate LDPs with porous materials such as covalent organic frameworks (COFs) or metal–organic frameworks (MOFs) offer promising pathways for photocatalytic CO_2 reduction. In such systems, LDPs function as light harvesters and charge generators, while the porous frameworks facilitate CO_2 adsorption and activation. Rational design of these composite architectures could simultaneously improve catalytic efficiency and moisture stability.

(iii) Device level integration and emerging applications: although theoretical studies suggest that LDPs could be suitable for photovoltaic devices, experimental demonstrations of efficient solar cells remain scarce. Future efforts should focus on optimizing device architectures, interfacial engineering, and defect passivation strategies to enable high-performance photovoltaic devices. In addition, emerging applications such as photocatalytic CO_2 reduction and photothermal energy conversion require further development of efficient materials and optimized reaction systems.

In summary, LDPs are a highly promising class of lead-free materials but realizing their full potential in energy conversion and advanced optoelectronics will require thorough compositional engineering, novel synthesis routes, and seamless integration at the device level. Achieving this will depend on a multidisciplinary strategy that merges theoretical modelling, cutting-edge characterization, and practical engineering. This review gives researchers a clear insight into designing compositions, synthesizing them and applying strategies to develop and commercialize high-performance lead-free LDPs.

Author contributions

Kavitha Hosamane: conceptualization, writing - original draft, writing review and editing; Sangita Das: formal analysis, writing review and editing, validation, visualization; Partha Pratim Das: conceptualization, supervision, validation, visualization, writing – original draft, writing review and editing.

Conflicts of interest

There are no conflicts to declare.

Data availability

No primary research results, software or code have been included and no new data were generated or analysed as part of this review.

Acknowledgements

The authors acknowledge financial support from the Manipal Academy of Higher education (MAHE), Manipal. K. H acknowledges the Dr T. M. A Pai PhD Fellowship, and P. P. D. acknowledges intramural research funding (IMF, Project Id: 10007846UTN: RG09241241) from MAHE.

References

1 C. Zhou, H. Lin, Q. He, L. Xu, M. Worku, M. Chaaban, S. Lee, X. Shi, M.-H. Du and B. Ma, *Mater. Sci. Eng., R*, 2019, **137**, 38–65.

2 T. Cai, L. Dube, P. Saghy, H. Yang and O. Chen, *Trends Chem.*, 2023, **5**, 29–44.

3 P. P. Mohanty, R. Ahuja and S. Chakraborty, *Nanotechnology*, 2022, **33**, 292501.

4 B. Vargas, G. RodrÍguez-López and D. Solis-Ibarra, *ACS Energy Lett.*, 2020, **5**, 3591–3608.

5 V. Hazra, A. Mandal and S. Bhattacharyya, *Chem. Sci.*, 2024, **15**, 7374–7393.

6 J. Y. Lee, P. Pandey, S. Lee, Q. Shen and D. W. Kang, *Chem. Eng. J.*, 2024, **491**, 152026.

7 A. K. Jena, A. Kulkarni and T. Miyasaka, *Chem. Rev.*, 2019, **119**, 3036–3103.

8 L. R. W. White, F. U. Kosasih, K. Ma, J. Fu, M. Feng, M. P. Sherburne, M. Asta, T. C. Sum, S. G. Mhaisalkar and A. Bruno, *ACS Energy Lett.*, 2024, **9**, 4450–4458.

9 Z. Li, L. Jiang, X. Rong, Q. Dong, H. Dong, L. Wang and G. Dong, *J. Phys. Chem. Lett.*, 2022, **13**, 815–821.

10 M. Singh, Akash and J. P. Tiwari, *ACS Appl. Energy Mater.*, 2024, **7**, 10212–10229.

11 V. Kumar, A. Kathiravan and M. A. Jhonsi, *Nano Energy*, 2024, **125**, 109523.

12 A. E. Magdalin, P. D. Nixon, E. Jayaseelan, M. Sivakumar, S. K. N. Devi, M. S. P. Subathra, N. M. Kumar and N. Ananthi, *Results Eng.*, 2023, **20**, 101438.

13 M. Wang, W. Wang, B. Ma, W. Shen, L. Liu, K. Cao, S. Chen and W. Huang, *Nanomicro Lett.*, 2021, **13**, 62.

14 P. Kumari, S. Prasanthkumar and L. Giribabu, *Sol. Energy*, 2024, **284**, 113049.

15 F. Bai, Y. Hu, Y. Hu, T. Qiu, X. Miao and S. Zhang, *Sol. Energy Mater. Sol. Cells*, 2018, **184**, 15–21.

16 S. Mishra, S. Sapru, S. N. Upadhyay, A. Singh, S. Pakhira and A. K. De, *J. Phys. Chem. C*, 2023, **127**, 1881–1890.

17 B. Saparov, F. Hong, J.-P. Sun, H.-S. Duan, W. Meng, S. Cameron, I. G. Hill, Y. Yan and D. B. Mitzi, *Chem. Mater.*, 2015, **27**, 5622–5632.

18 P. Kumar and A. Kumar, *J. Mater. Sci.: Mater. Electron.*, 2023, **34**, 1810.

19 S. Ghosh, H. Shankar and P. Kar, *Mater. Adv.*, 2022, **3**, 3742–3765.

20 S. Umer, M. I. Khan, A. Ullah, Ihtisham-ul-haq, M. Asad, I. Kebaili, W. Mnif, Z. Algarni and M. I. Saleem, *Opt. Mater.*, 2024, **156**, 115896.

21 A. Ullah, W. ur Rehman, M. I. Khan and N. S. A. EL-Gawaad, *J. Solgel Sci. Technol.*, 2024, **112**, 814–825.

22 S. Zhang, G. Liu, B. Teng and S. Ji, *CrystEngComm*, 2025, **27**, 3416–3432.

23 M. Ghasemi, P. Karsili, A. Mishra, M. R. Golobostanfard and J. V. Milić, *Adv. Energy Mater.*, 2025, **15**, 1–27.

24 B. Vargas, R. Torres-Cadena, J. Rodríguez-Hernández, M. Gembicky, H. Xie, J. Jiménez-Mier, Y. S. Liu, E. Menéndez-Proupin, K. R. Dunbar, N. Lopez, P. Olalde-Velasco and D. Solis-Ibarra, *Chem. Mater.*, 2018, **30**, 5315–5321.

25 B. Vargas, E. Ramos, E. Pérez-Gutiérrez, J. C. Alonso and D. Solis-Ibarra, *J. Am. Chem. Soc.*, 2017, **139**, 9116–9119.

26 C. Zhao, Y. Gao and J. Qiu, *Inorg. Chem.*, 2023, **62**, 17382–17389.

27 R. Nie, R. R. Sumukam, S. H. Reddy, M. Banavoth and S. Il Seok, *Energy Environ. Sci.*, 2020, **13**, 2363–2385.

28 N. Singhal, R. Chakraborty, P. Ghosh and A. Nag, *Chem. – Asian J.*, 2018, **13**, 2085–2092.

29 X. D. Wang, N. H. Miao, J. F. Liao, W. Q. Li, Y. Xie, J. Chen, Z. M. Sun, H. Y. Chen and D. Bin Kuang, *Nanoscale*, 2019, **11**, 5180–5187.

30 T. Cai, W. Shi, S. Hwang, K. Kobbekaduwa, Y. Nagaoka, H. Yang, K. Hills-Kimball, H. Zhu, J. Wang, Z. Wang, Y. Liu, D. Su, J. Gao and O. Chen, *J. Am. Chem. Soc.*, 2020, **142**, 11927–11936.

31 P. M. Jayasankar, A. K. Pathak, S. P. Madhusudanan, S. Murali and S. K. Batabyal, *Mater. Lett.*, 2020, **263**, 127200.

32 T. Cai, W. Shi, D. J. Gosztola, K. Kobbekaduwa, H. Yang, N. Jin, Y. Nagaoka, L. Dube, J. Schneider, S. Hwang, J. Gao, X. Ma and O. Chen, *Matter*, 2021, **4**, 2936–2952.

33 P. P. Ashitha, M. Joshi, D. Verma, S. Jadhav, A. R. Choudhury and D. Jana, *ACS Appl. Nano Mater.*, 2021, **4**, 1305–1313.

34 A. Mandal, A. Mondal, R. Bhattacharyya and S. Bhattacharyya, *Nanotechnology*, 2022, **33**, 415403.
35 S. Parveen, L. T. Manamel, A. Mukherjee, S. Sagar and B. C. Das, *Adv. Mater. Interfaces*, 2022, **9**, 2200562.
36 D. Wu, C. Tian, J. Zhou, Y. Huang, J. Lai, B. Gao, P. He, Q. Huang and X. Tang, *Carbon Neutralization*, 2022, **1**, 298–305.
37 H.-J. Zhang, T. Song, X.-X. Liu, M.-Z. Chen, B. Ma, H.-Z. Huang, X.-P. Zhai, Q. Wang, Y.-L. Tang and H.-L. Zhang, *J. Mater. Chem. C*, 2023, **11**, 14127–14133.
38 V. Hoseinpour, Z. Shariatinia and L. Echegoyen, *Mater. Res. Bull.*, 2023, **159**, 112088.
39 S. Mishra, S. Sapru, S. N. Upadhyay, A. Singh, S. Pakhira and A. K. De, *J. Phys. Chem. C*, 2023, **127**, 1881–1890.
40 J. U. Balderas-Aguilar, C. Falcony-Guajardo, I. A. Garduño-Wilches, M. Á. Aguilar-Frutis, N. Hernández-Como, I. E. Martínez-Merlín, M. García-Hipólito and J. C. Alonso-Huitrón, *J. Mater. Chem. C*, 2023, **11**, 16214–16224.
41 K. Zhang, Y. Zhang, D. Zhou, Y. Yang, Z. Yang, Z. Song, J. Zhang, Q. Wang and J. Qiu, *J. Alloys Compd.*, 2024, **976**, 173283.
42 Y. Wang, Y. Ji, Y. Yang, Z. Chen, H. Sun, X. Wang, Z. Zou and H. Huang, *ACS Energy Lett.*, 2024, **9**, 336–345.
43 P. Kumar and A. Kumar, *Silicon*, 2024, **16**, 3343–3357.
44 S. Mishra, A. Gurjar and A. K. De, *J. Phys. Chem. C*, 2025, **129**, 5156–5163.
45 Y. Chang, X. Gan, J. Liao, L. Du, L. Guo, Z. Wen and H. Liu, *J. Solid State Chem.*, 2025, **347**, 125295.
46 V. Sridhar, C. Wu and S. Chattopadhyay, *ACS Appl. Mater. Interfaces*, 2025, **17**, 39584–39594.
47 J. A. Sarkar, M. J. Pulikkathumbayil, V. P. Veena and M. Aslam, *ACS Appl. Nano Mater.*, 2025, **8**, 17121–17132.
48 Y.-P. Lin, S. Hu, B. Xia, K.-Q. Fan, L.-K. Gong, J.-T. Kong, X.-Y. Huang, Z. Xiao and K.-Z. Du, *J. Phys. Chem. Lett.*, 2019, **10**, 5219–5225.
49 B. Vargas, D. T. Reyes-Castillo, E. Coutino-Gonzalez, C. Sánchez-Aké, C. Ramos, C. Falcony and D. Solis-Ibarra, *Chem. Mater.*, 2020, **32**, 9307–9315.
50 N. P. Holzapfel, J. D. Majher, T. A. Strom, C. E. Moore and P. M. Woodward, *Chem. Mater.*, 2020, **32**, 3510–3516.
51 J.-H. Wei, J.-F. Liao, X.-D. Wang, L. Zhou, Y. Jiang and D.-B. Kuang, *Matter*, 2020, **3**, 892–903.
52 H. Yang, W. Shi, T. Cai, K. Hills-Kimball, Z. Liu, L. Dube and O. Chen, *Nanoscale*, 2020, **12**, 23191–23199.
53 S. He, S. Fang, T. Han, T. Lang, M. Cai, H. You, L. Peng, S. Cao, B. Liu, Q. Qiang, J. Chen and B. Lei, *J. Phys. Chem. C*, 2021, **125**, 16938–16945.
54 Y. Ma, L. Zhang, Y. Tang, S. Wu, M. L. Tong, K. Wang, B. Zou and M. R. Li, *ACS Appl. Energy Mater.*, 2021, **4**, 7513–7518.
55 T. Bai, B. Yang, J. Chen, D. Zheng, Z. Tang, X. Wang, Y. Zhao, R. Lu and K. Han, *Adv. Mater.*, 2021, **33**, 2007215.
56 M. B. Gray, J. D. Majher, N. P. Holzapfel and P. M. Woodward, *Chem. Mater.*, 2021, **33**, 2165–2172.
57 Arramel, F. Maddalena, M. H. Mahyuddin, X. Yin, C. S. Tang, M. K. Agusta, M. F. Sahdan, C. Diao, C. Dang, M. D. Birowosuto, A. T. S. Wee and A. Rusydi, *Mater. Today Energy*, 2022, **24**, 100921.
58 H. Yang, T. Cai, L. Dube and O. Chen, *Chem. Sci.*, 2022, **13**, 4874–4883.
59 J. Li, J. Xiao, T. Lin, Z. Yan and X. Han, *J. Mater. Chem. C*, 2022, 7626–7632.
60 J. Lin, P. Dang, G. Zhang, W. Yang, H. Lian and G. Li, *Research Square*, 2022, 1–21.
61 H. Liu, H. Hafeez, D. B. Cordes, A. M. Z. Slawin, G. Peters, S. L. Lee, I. D. W. Samuel and F. D. Morrison, *Inorg. Chem.*, 2023, **62**, 3629–3636.
62 C. Zhao, Y. Gao and J. Qiu, *Inorg. Chem.*, 2023, **62**, 17382–17389.
63 C. Wang, J. Xiao, Z. Yan, X. Niu, T. Lin, Y. Zhou, J. Li and X. Han, *Nano Res.*, 2023, **16**, 1703–1711.
64 P. Dang, G. Zhang, W. Yang, H. Lian, G. Li and J. Lin, *Chem. Mater.*, 2023, **35**, 1640–1650.
65 J. Liu, Q. Hu, H. Yu, H. Xu, J. Yu, Q. Han and W. Wu, *Inorg. Chem.*, 2023, **62**, 9111–9119.
66 H. Wei, Z. Li, H. Wang, Y. Yang, P. Cheng, P. Han, R. Zhang, F. Liu, P. Zhou and K. Han, *J. Energy Chem.*, 2023, **82**, 18–24.
67 Z. Chen, F. Zhang, D. Yang, H. Ji, X. Chen, D. Wu, X. Li, Y. Zhang and Z. Shi, *Nano Res.*, 2024, **17**, 3068–3078.
68 B. Gao, C. Tian, L. Guo, J. Zhou, Z. Wang, C. Fu, H. Ran, W. Chen, Q. Huang, D. Wu, X. Tang and Z. Luo, *Adv. Sci.*, 2024, **11**, 2307543.
69 A. Singh, C. Barman and S. S. K. Raavi, *Opt. Mater.*, 2025, **166**, 117182.
70 Y. Huang, Y. Liu, Y. Liu, X. Tan, Y. Wang, Q. Xiao, X. Tong, J. Pan, Z. Yu, Z. Yao and Y. Hou, *Chem. Eng. J.*, 2025, **518**, 164734.
71 W. Chen, Y. Huang, D. Wu, H. Ran, Y. Liu, L. Gao, W. Zhang, Q. Huang and X. Tang, *Inorg. Chem.*, 2025, **64**, 8532–8543.
72 Y. Liu, W. Chen, Y. Huang, D. Wu, H. Ran, L. Gao, W. Zhang, Y. Liu and X. Tang, *ACS Appl. Energy Mater.*, 2025, **8**, 6501–6509.
73 H. Mai, X. Li, J. Lu, X. Wen, T. C. Le, S. P. Russo, D. Chen and R. A. Caruso, *J. Am. Chem. Soc.*, 2023, **145**, 17337–17350.
74 J. Liu, A. A. Vedernikova, Q. Xue, H. Gao, X. Xie, J. Xie, E. V. Ushakova, H. Huang and X. Zhang, *Adv. Sci.*, 2025, **12**, 1–8.
75 M. Liu, S. K. Matta, H. Ali-Löytty, A. Matuhina, G. K. Grandhi, K. Lahtonen, S. P. Russo and P. Vivo, *Nano Lett.*, 2022, **22**, 311–318.
76 M. Liu, S. K. Matta, T. Al Said, J. Liu, A. Matuhina, B. Al-Anesi, H. Ali-Löytty, K. Lahtonen, S. P. Russo and P. Vivo, *Small*, 2024, **20**, 2401051.
77 Yukta, S. Rahman, Q. Shi, T. A. Said, S. K. Matta, T. Hu, W. Wang, A. Opis-Basilio, K. Ray, K. A. Dick, T. Pullerits and M. Liu, *Small Struct.*, 2025, **6**, 2500179.
78 M. P. Hautzinger, W. Mihalyi-Koch and S. Jin, *Chem. Mater.*, 2024, **36**, 10408–10420.
79 W. Gao, C. Chen, C. Ran, H. Zheng, H. Dong, Y. Xia, Y. Chen and W. Huang, *Adv. Funct. Mater.*, 2020, **30**(34), 2000794.

80 M. M. Byranvand, C. Otero-Martínez, J. Ye, W. Zuo, L. Manna, M. Saliba, R. L. Z. Hoye and L. Polavarapu, *Adv. Opt. Mater.*, 2022, **10**(14), 2200423.

81 J. Xu, J. B. Liu, J. Wang, B. X. Liu and B. Huang, *Adv. Funct. Mater.*, 2018, **28**, 1–10.

82 Z. Liu, S. Liu, X. Zhang, H. Hao, X. Chang, Z. Shen, L. Kong, Q. Zhang and L. Li, *J. Phys. Chem. Lett.*, 2025, **16**, 7443–7450.

83 B. Vargas, R. Torres-Cadena, D. T. Reyes-Castillo, J. Rodríguez-Hernández, M. Gembicky, E. Menéndez-Proupin and D. Solis-Ibarra, *Chem. Mater.*, 2020, **32**, 424–429.

84 N. Daem, A. Maho, P. Colson, G. Spronck, C. Malherbe, T. H. Hoang, M. N. Ghazzal, G. He, F. Lang, R. Cloots and J. Dewalque, *Next Mater.*, 2025, **8**, 0–11.

85 K. M. Boopathi, P. Karuppuswamy, A. Singh, C. Hanmandlu, L. Lin, S. A. Abbas, C. C. Chang, P. C. Wang, G. Li and C. W. Chu, *J. Mater. Chem. A Mater.*, 2017, **5**, 20843–20850.

86 Z. Liu, D. Liu, H. Chen, L. Ji, H. Zheng, Y. Gu, F. Wang, Z. Chen and S. Li, *Nanoscale Res. Lett.*, 2019, **14**, 304.

87 J. J. Gallardo, M. Barea-Sepúlveda, T. Aguilar, R. Alcántara, C. Fernández-Lorenzo and J. Navas, *Mater. Res. Bull.*, 2019, **119**, 110528.

88 J. Wen, K. Rong, L. Jiang, C. Wen, B. Wu, B. Sa, Y. Qiu and R. Ahuja, *Nano Energy*, 2024, **128**, 109802.

89 T. Cai, W. Shi, S. Hwang, K. Kobbekaduwa, Y. Nagaoka, H. Yang, K. Hills-Kimball, H. Zhu, J. Wang, Z. Wang, Y. Liu, D. Su, J. Gao and O. Chen, *J. Am. Chem. Soc.*, 2020, **142**, 11927–11936.

90 H. Mai, X. Li, J. Lu, X. Wen, T. C. Le, S. P. Russo, D. Chen and R. A. Caruso, *J. Am. Chem. Soc.*, 2023, **145**, 17337–17350.

91 J.-H. Wei, J.-F. Liao, X.-D. Wang, L. Zhou, Y. Jiang and D.-B. Kuang, *Matter*, 2020, **3**, 892–903.

92 Y. Chen, H. Zhu, D. Babaian, C. Dzorkpata, A. Grigoriev, Z. Wang, S. Wheat, S. Guha and P. Zhu, *Adv. Mater.*, 2025, **37**, 2500083.

93 A. Sawahreh, T. Binyamin, J. Jiang, O. Millo, O. Goldberg, D. Azulay, R. Pachter and L. Etgar, *Nanoscale*, 2022, **14**, 3487–3495.

94 H. Liu, H. Hafeez, D. B. Cordes, A. M. Z. Slawin, G. Peters, S. L. Lee, I. D. W. Samuel and F. D. Morrison, *Inorg. Chem.*, 2023, **62**, 3629–3636.

95 C. Zhang, L. He, J. Li, K. Shi, P. Chang, Y. Zheng, Y. Yang, D. Zhou and J. Qiu, *J. Lumin.*, 2026, **289**, 121642.

96 E. Sartori, M. Campolucci, D. Baranov, M. Zeng, S. Toso, G. Divitini, M. Ferretti, Z. Hens, L. Manna and F. Locardi, *Nanoscale*, 2022, **14**, 305–311.

97 W. Tao, H. Wu, L. Xiao and Z. Xiao, *Mater. Today Energy*, 2025, **54**, 102101.

98 B. Vargas, E. Coutiño-Gonzalez, O. Ovalle-Encinia, C. Sánchez-Aké and D. Solis-Ibarra, *J. Phys. Chem. Lett.*, 2020, **11**, 10362–10367.

99 H. Lin, S. Talebi, W. MacSwain, V. Vanshika, A. Chakraborty and W. Zheng, *ACS Nano*, 2025, **19**, 14941–14953.

100 N. S. M. Viswanath and W. B. Im, *ACS Appl. Opt. Mater.*, 2025, **3**, 578–600.

101 V. V. Klepov, K. A. Pace, A. A. Berseneva, J. B. Felder, S. Calder, G. Morrison, Q. Zhang, M. J. Kirkham, D. S. Parker and H.-C. zur Loye, *J. Am. Chem. Soc.*, 2021, **143**, 11554–11567.

102 J. Xu, J. B. Liu, B. X. Liu and B. Huang, *Adv. Funct. Mater.*, 2021, **31**, 1–8.

103 D. Han, T. Zhang and S. Chen, *J. Phys.:Condens. Matter*, 2020, **32**, 225705.

104 C. Feng, Q. Zhao, C. Wu, X. Luo, S. Li, D. Li, G. Tang and G. Zhang, *J. Phys. Chem. Lett.*, 2022, **13**, 1077–1084.

105 S. Mishra, A. Gurjar and A. K. De, *J. Phys. Chem. C*, 2025, **129**, 5156–5163.

106 S. Mishra, S. Sapru, S. N. Upadhyay, A. Singh, S. Pakhira and A. K. De, *J. Phys. Chem. C*, 2023, **127**, 1881–1890.

107 A. Santhiran, J. Zhu, Y. Chen, E. Gi, X. Zhou, X. Peng, X. Kong, J. Vela and A. Rossini, *ChemRxiv*, 2025, preprint, DOI: 10.26434/chemrxiv-2025-3wjpt.

108 K. C. Chou, R. Wu, O. Chen and J. Z. Zhang, *J. Phys. Chem. Lett.*, 2025, **16**, 11421–11427.

109 F. Li, L. Cao, S. Shi, H. Gao, L. Song, C. Geng, W. Bi and S. Xu, *Angew. Chem., Int. Ed.*, 2019, **58**, 17631–17635.

110 Y. Zheng, H. Lv, H. Q. Wang, C. Geng and S. Xu, *J. Phys. Chem. Lett.*, 2024, **15**, 4040–4046.

111 J. Xie, L. Wu, M. Cao, Q. Zhong, Y. Zeng, C. Ni, Q. Qian, X. Zhang and H. Huang, *Adv. Mater. Technol.*, 2022, **7**, 1–8.

112 L. Cao, S. Shi, F. Li, Z. Tian, S. Xu and C. Geng, *Chem. Eng. J.*, 2022, **434**, 134693.

113 T. T. Tran, T. T. Tran, C. A. Pocs, Y. Zhang, Y. Zhang, M. J. Winiarski, M. J. Winiarski, J. Sun, M. Lee, T. M. McQueen and T. M. McQueen, *Phys. Rev. B*, 2020, **101**, 235107.

114 N. P. Holzapfel, J. D. Majher, T. A. Strom, C. E. Moore and P. M. Woodward, *Chem. Mater.*, 2020, **32**, 3510–3516.

115 H.-J. Zhang, T. Song, X.-X. Liu, M.-Z. Chen, B. Ma, H.-Z. Huang, X.-P. Zhai, Q. Wang, Y.-L. Tang and H.-L. Zhang, *J. Mater. Chem. C*, 2023, **11**, 14127–14133.

116 D. Zheng, F. Raffin, P. Volovitch and T. Pauporté, *Nat. Commun.*, 2022, **13**, 6655.

117 K. M. Boopathi, P. Karuppuswamy, A. Singh, C. Hanmandlu, L. Lin, S. A. Abbas, C. C. Chang, P. C. Wang, G. Li and C. W. Chu, *J. Mater. Chem. A*, 2017, **5**, 20843–20850.

118 D. Zhao, B. Wang, C. Liang, T. Liu, Q. Wei, S. Wang, K. Wang, Z. Zhang, X. Li, S. Peng and G. Xing, *Sci. China Mater.*, 2020, **63**, 1518–1525.

119 S. Wang, D. Han, C. Maheu, Z. Xu, A. Biewald, H. Illner, R. Hooijer, T. Mayer, A. Hartschuh, H. Ebert and T. Bein, *APL Materials*, 2023, **11**, 041110.

120 J. R. Bautista-Quijano, O. Telschow, F. Paulus and Y. Vaynzof, *Chem. Commun.*, 2023, **59**, 10588–10603.

121 Q. Chen, A. K. Singh, H. Alghathami, X. Liu, K. Huang, A. G. Thomas, R. J. Curry, L. J. Phillips and A. J. Hughes, *Green Chem.*, 2025, **27**, 7532–7543.

122 M. Zhang, Z. Wang, B. Zhou, X. Jia, Q. Ma, N. Yuan, X. Zheng, J. Ding and W. Zhang, *Solar RRL*, 2018, **2**, 1700213.

123 Y. Cao, Z. Liu, T. Liu, K. Ou, Y. Cui, Y. Ni, Y. Xia and H. Wang, *J. Lumin.*, 2025, **286**, 121429.

124 Y. Wang, J. Chen, Y. Zhang, P. Lv, J. Pan, M. Hu, W. L. Tan, Z. Ku, Y.-B. Cheng, A. N. Simonov and J. Lu, *Adv. Mater.*, 2024, **36**, 2412021.
125 J. H. Hernández, J. U. Balderas Aguilar, L. A. Becerril Landeros, C. Falcony and I. E. Martinez Merlin, *Cryst. Growth Des.*, 2025, **25**, 253–263.
126 Z. Wang, M. Lyu, B. W. Zhang, M. Xiao, C. Zhang, E. Q. Han and L. Wang, *Small Methods*, 2025, **9**, 1–35.
127 X.-D. Wang, N.-H. Miao, J.-F. Liao, W.-Q. Li, Y. Xie, J. Chen, Z.-M. Sun, H.-Y. Chen and D.-B. Kuang, *Nanoscale*, 2019, **11**, 5180–5187.
128 T. Du, F. Richheimer, K. Frohna, N. Gasparini, L. Mohan, G. Min, W. Xu, T. J. MacDonald, H. Yuan, S. R. Ratnasingham, S. Haque, F. A. Castro, J. R. Durrant, S. D. Stranks, S. Wood, M. A. McLachlan and J. Briscoe, *Nano Lett.*, 2022, **22**, 979–988.
129 M. Li, W. Li and H. Wei, 2025, DOI: 10.1002/adpr.202400095.
130 Y. He, L. Xu, C. Yang, X. Guo and S. Li, *Nanomaterials*, 2021, **11**, 2321.
131 H. Na, M. Qiang Li, J. Cha, S. Kim, H. Jin, D. Baek, M. Kyong Kim, S. Sim, M. Lee, M. Kim, J. Lim, J. Lee and M. Kim, *Appl. Surf. Sci.*, 2023, **626**, 157209.
132 C. Kan, C. Luo and Y. Hou, *Energy Environ. Sci.*, 2026, 1101–1123.
133 K. M. Sadat, M. K. Hossain, M. S. Uddin, P. Prabhu, A. Aggarwal, K. Gopalakrishna, P. S. Kiran, A. K. Mishra, S. K. Shah, S. Islam, A. M. S. Alhuthali, M. H. Abdellattif and V. K. Mishra, *Sci. Rep.*, 2025, **15**, 1–18.
134 Y. Wang, Y. Ji, Y. Yang, Z. Chen, H. Sun, X. Wang, Z. Zou and H. Huang, *ACS Energy Lett.*, 2024, **9**, 336–345.
135 S. C. Yadav, V. Manjunath, A. Srivastava, R. S. Devan and P. M. Shirage, *Opt. Mater.*, 2022, **132**, 112676.
136 W. Yang, W. Li, T. Li and Q. Liu, *Renew. Energy*, 2026, **256**, 124022.
137 K. Zhang, Y. Zhang, D. Zhou, Y. Yang, Z. Yang, Z. Song, J. Zhang, Q. Wang and J. Qiu, *J. Alloys Compd.*, 2024, **976**, 173283.
138 G. N. Liu, R. Y. Zhao, B. Xu, Y. Sun, X. M. Jiang, X. Hu and C. Li, *ACS Appl. Mater. Interfaces*, 2020, **12**, 54694–54702.
139 Z. Cui, P. Wang, Y. Wu, X. Liu, G. Chen and P. Gao, *Appl. Catal., B*, 2022, **310**, 121375.
140 D. Lan, D. Yongping, B. Fenghua, C. Gonglai, Z. Shuwei, Y. Xiaoxue, L. Huiqin and W. Xiaojing, *Inorg. Chem.*, 2023, **62**, 2289–2303.
141 Q. M. Sun, J. J. Xu, F. F. Tao, W. Ye, C. Zhou, J. H. He and J. M. Lu, *Angew. Chem., Int. Ed.*, 2022, **61**, e202200872.
142 Z. Xie and Y. H. Ng, *Energy Fuels*, 2025, **40**, 1831–1883.